HHS Public Access

Author manuscript

Cell Rep. Author manuscript; available in PMC 2024 January 24.

Published in final edited form as:

Cell Rep. 2023 December 26; 42(12): 113529. doi:10.1016/j.celrep.2023.113529.

Molecular determinants of the crosstalk between endosomal microautophagy and chaperone-mediated autophagy

Gregory J. Krause[1,2], **Philipp Kirchner**[1,2], **Barbara Stiller**[1,2], **Kateryna Morozova**[3], **Antonio Diaz**[1,2], **Kuei-Ho Chen**[4,5,6], **Nevan J. Krogan**[4,5,6], **Esperanza Agullo-Pascual**[7], **Cristina C. Clement**[3], **Kristen Lindenau**[1,2], **Danielle L. Swaney**[4,5,6], **Shilpa Dilipkumar**[7], **Jose Javier Bravo-Cordero**[8,9], **Laura Santambrogio**[3,*], **Ana Maria Cuervo**[1,2,10,*]

[1]Department of Developmental and Molecular Biology, Albert Einstein College of Medicine, Bronx, NY 10461, USA

[2]Institute for Aging Studies, Albert Einstein College of Medicine, Bronx, NY 10461, USA

[3]Department of Radiation Oncology, Weill Cornell School of Medicine, New York, NY 10021, USA

[4]Department of Cellular and Molecular Pharmacology, University of California, San Francisco, San Francisco, CA 94158, USA

[5]The J. David Gladstone Institutes, San Francisco, CA 94158, USA

[6]Quantitative Biosciences Institute (QBI), University of California, San Francisco, San Francisco, CA 94158, USA

[7]Microscopy CoRE, Dean's CoREs, Icahn School of Medicine at Mount Sinai, New York, NY 10029, USA

[8]Department of Medicine, Icahn School of Medicine at Mount Sinai, New York, NY 10029, USA

[9]The Tisch Cancer Institute, Icahn School of Medicine at Mount Sinai, New York, NY 10029, USA

[10]Lead contact

SUMMARY

Chaperone-mediated autophagy (CMA) and endosomal microautophagy (eMI) are pathways for selective degradation of cytosolic proteins in lysosomes and late endosomes, respectively. These autophagic processes share as a first step the recognition of the same five-amino-acid motif in

*Correspondence: las4011@med.cornell.edu (L.S.), ana-maria.cuervo@einsteinmed.edu (A.M.C.).

AUTHOR CONTRIBUTIONS

G.J.K. designed, performed, and analyzed experiments and wrote the first draft of the manuscript; B.S. and P.K. performed LE/MVB and eMI reporter experiments; K.M. performed Hsc70 co-immunoprecipitation studies; A.D. performed high-content microscopy and protein degradation studies; K.L. performed siRNA-knockdown experiments; K.-H.C., N.J.K., and D.L.S. performed and analyzed proteomics; E.A.-P., S.D., and J.J.B.-C. advised and assisted with STED microscopy experiments; C.C.C. performed mass spectrometry and analysis; and L.S. and A.M.C. conceived, coordinated, and directed the study, contributed to manuscript writing, and edited the final version of the manuscript.

INCLUSION AND DIVERSITY

We support inclusive, diverse, and equitable conduct of research.

SUPPLEMENTAL INFORMATION

Supplemental information can be found online at https://doi.org/10.1016/j.celrep.2023.113529.

substrate proteins by the Hsc70 chaperone, raising the possibility of coordinated activity of both pathways. In this work, we show the existence of a compensatory relationship between CMA and eMI and identify a role for the chaperone protein Bag6 in triage and internalization of eMI substrates into late endosomes. Association and dynamics of Bag6 at the late endosome membrane change during starvation, a stressor that, contrary to other autophagic pathways, causes a decline in eMI activity. Collectively, these results show a coordinated function of eMI with CMA, identify the interchangeable subproteome degraded by these pathways, and start to elucidate the molecular mechanisms that facilitate the switch between them.

In brief

Krause et al. show compensatory mechanisms between chaperone-mediated autophagy and endosomal microautophagy (eMI) facilitated by Bag6, which is required for substrate internalization by eMI. Changes in Bag6 association with late endosomes contribute to the inhibitory effect of starvation on eMI identified in this work.

Graphical Abstract

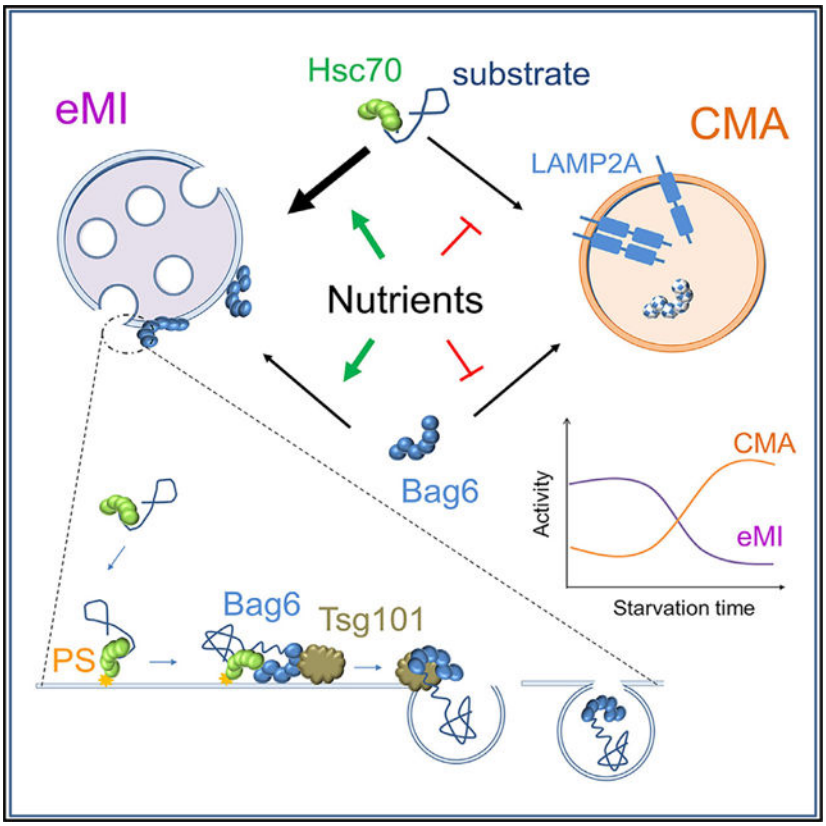

INTRODUCTION

Autophagy is an essential component of the proteostasis network that maintains the cellular proteome.[1,2] Defects in autophagic pathways have been associated with aging[3–5] and with a variety of diseases, including neurodegenerative conditions[6–8] and cancer.[9,10]

Several types of autophagy co-exist in mammalian cells. Macroautophagy degrades cellular material sequestered in autophagosomes upon fusion with lysosomes or late endosomes.[8,11] Chaperone-mediated autophagy (CMA) degrades proteins bearing a pentapeptide KFERQ-like motif that, when recognized by the heat-shock cognate protein of 70 kDa (Hsc70),[12] are delivered to lysosomes for binding to the lysosome-associated membrane protein type 2A (LAMP-2A; L2A)[13] and subsequent direct translocation across the membrane for luminal degradation.[14] Microautophagy, originally described in yeast,[15] occurs in mammals via invaginations in the membranes of late endosomes/multivesicular bodies (LE/MVBs) (reviewed in Tekirdag and Cuervo[16,17] and Wang et al.[17]). In endosomal microautophagy (eMI),[18] the subtype of microautophagy with the highest similarity to CMA, substrates are also targeted for degradation upon recognition of a KFERQ-like motif by Hsc70.[18] However, in eMI, Hsc70 binds to phosphatidylserine in the LE/MVB membrane, triggering the loading of substrate into vesicles that form on the surface of the organelle in an endosomal sorting complexes required for transport (ESCRT)-dependent manner.[19]

Although eMI and CMA share the same cargo recognition mechanism, it is unclear how substrate proteins are targeted to lysosomes or LE/MVBs. Recently, we showed that upon blockage of CMA, Tau, a pathogenic protein degraded by CMA, is released extracellularly in an eMI-dependent manner.[20] However, whether this rerouting from CMA to eMI occurs for other proteins and the extent of the proteome shared between these pathways remain unknown.

In this work, we show a compensatory relationship between eMI and CMA. Using comparative proteomics, we demonstrate that blockage of CMA leads to rerouting of a subset of CMA substrates to eMI. Furthermore, we identify that the chaperone Bag6 mediates eMI of a subset of the proteome. Finally, we show that starvation, known to upregulate other autophagy pathways,[1,21] inhibits eMI activity, in part because of reduced association and changes in the topology of Bag6 in LE/MVBs under these conditions. Together, these findings outline physiological conditions in which eMI activity changes to contribute to remodeling of the cellular proteome.

RESULTS

CMA and eMI exhibit a compensatory relationship

Degradation through CMA and eMI requires Hsc70 recognition of a KFERQ-like motif in substrate proteins followed by targeting to lysosomes or LE/MVBs, respectively. To determine if the same substrates can be degraded by both pathways and with comparable efficiency, we used established *in vitro* assays with isolated intact LE/MVBs[18] and the subpopulation of lysosomes active for CMA (CMA^+ lysosomes)[22] (Figure S1A shows enrichment for Rab7 in LE/MVBs and for ATP6V1B and GBA in lysosomes and the presence of Hsc70 in CMA^+ but not CMA^- lysosomes). Any preparation with >10% membrane breakage (determined as leakage of β-hexosaminidase) was discarded. We incubated these organelles with the KFERQ-bearing proteins GAPDH, LRRK2, and Tau or with Cyclophilin A, which lacks a KFERQ-like motif and is degraded in LE/MVBs through non-selective eMI (Figures 1A and 1B). Addition of inhibitors of endolysosomal proteases, which permits differentiating substrate binding (no inhibitors)

from internalization/degradation (with inhibitors), revealed that LE/MVBs and CMA$^+$ lysosomes can bind and degrade the same substrate proteins, albeit with different efficiencies (Figures 1A–1C). GAPDH and LRRK2 bound to both organelles but showed higher degradation in lysosomes, in agreement with most eMI substrates being degraded upon LE/MVB fusion with lysosomes.[18] Internalization/degradation of Cyclophilin A by both pathways was negligible (Figures 1A–1C). Interestingly, Tau is the first protein that shows similar efficiencies of degradation by CMA$^+$ lysosomes and LE/MVBs, suggesting that a subset of eMI substrates may be degraded in LE/MVBs (Figure 1C).

A compensatory relationship between macroautophagy and CMA, where blockage of one pathway leads to upregulation of the other, has been described.[23–26] To explore a possible similar relationship between eMI and CMA, we used mouse fibroblasts as control (Ctr) or knocked down for L2A (L2A(−)), to block CMA, and measured eMI activity with the KFERQ-Split Venus reporter.[27,28] In this reporter, two self-complementing fragments of the Venus protein fluoresce only once they coincide in the confined space of an intraluminal vesicle of LE/MVBs (positive for LAMP-1 and the ESCRT proteins Vps4 and Tsg101) (Figures S1B–S1E, also showing no co-localization with early endosomes [EEA1$^+$] or protein aggregates [ubiquitin$^+$]). eMI activity (number of fluorescent puncta per cell section) was significantly higher in CMA-deficient cells compared with control cells (Figure 1D). Conversely, cells knocked down for Vps4A/B to block eMI[18] displayed higher CMA activity with the photoswitchable KFERQ-Dendra CMA reporter[29,30] (Figure 1E). CMA upregulation was not due to impaired macroautophagy, since, as reported before,[20] the degree of Vps4 knockdown required to inhibit eMI did not affect the endolysosomal system (Figures S2A and S2B) nor did it inhibit macroautophagy (Figures S2C–S2G). In fact, macroautophagy was elevated in these cells, as demonstrated through (1) morphometric analysis (significant increase in autolysosomes) (Figures S2C and S2D), (2) elevated macroautophagy-dependent degradation of long-lived proteins (Figure S2E), and (3) higher macroautophagy flux using the fluorescent reporter mCherry-GFP-LC3 to monitor conversion of dual-fluorescent puncta (autophagosomes) into mCherry$^+$/GFP$^-$ puncta (autolysosomes) (Figures S2F and S2G).

To determine if eMI upregulation upon CMA blockage was due to increased internalization/degradation by LE/MVBs, we isolated LE/MVBs from the livers of mice that were wild type (WT) or knocked out for LAMP-2A (L2AKO)[26] (Figures S3A–S3C show comparability of LE/MVB fractions from both genotypes). Incubation of intact LE/MVBs with a pool of radiolabeled proteins revealed higher (>40% increase) eMI internalization/degradation of these proteins in LE/MVBs from CMA-incompetent mice (Figure 1F, top). These differences were no longer detected when LE/MVB membranes were disrupted to allow access of enzymes to the radiolabeled substrates, suggesting that the increase in eMI is due more to substrate internalization rather than higher protease activity (Figure 1F, bottom). Interestingly, the *in vitro* reconstitution system revealed higher internalization/degradation of GAPDH by LE/MVBs from CMA-deficient mice, but not of Tau (Figures 1G and 1H). Cyclophilin A exhibited reduced LE/MVB internalization/degradation upon CMA blockage, supporting the idea that enhanced internalization was specific for KFERQ-bearing substrates.

The differing impact of CMA blockage on eMI of GAPDH and Tau suggests that CMA blockage may result in qualitative changes in the proteome degraded by eMI to accommodate rerouted CMA substrates. To explore this possibility, we performed quantitative proteomics of LE/MVBs isolated from WT or L2AKO mouse livers. We injected half of the mice with leupeptin to inhibit LE/MVB proteases and identify endogenous proteins degraded inside (those with ≥20% abundance increase upon leupeptin injection[25]) (Figure 2A). Of 2,284 proteins identified in WT LE/MVBs, 1,738 were degraded in this compartment (Figure S3D). We discriminated cargo arriving to LE/MVBs from cytosol or via endocytosis, pinocytosis, or phagocytosis using Gene Ontology (GO) analysis and eliminating proteins under the terms “extracellular space’’ and “plasma membrane” (Figure S3E). Cytosolic proteins can arrive to LE/MVBs by fusion with autophagosomes or through different microautophagy-related processes, but a requirement for a KFERQ-like motif in their sequence is unique for eMI. Sequence analysis revealed that 45.3% of LE/MVB-degraded intracellular proteins contained a canonical KFERQ-like motif and 31.8% had the potential to generate motifs through phosphorylation or acetylation.[31] Because CMA and eMI degrade not only damaged proteins for quality control but also fully functional proteins to terminate their cellular functions, we performed STRING[32] and REACTOME[33] pathway enrichment analysis to identify cellular pathways that might be regulated by eMI. eMI substrates grouped into GO terms related to general metabolism and metabolism of RNA, cellular response to stimuli such as nutrients, cell death, vesicular trafficking, and protein localization and included some autophagy-related proteins (Figure 2B, top).

Similar analysis identified a lower number of proteins (25% less) undergoing degradation in LE/MVBs from L2AKO animals but similar intra- and extracellular distribution (71.7% and 28.3%, respectively) (Figures S3D and S3E). Comparative analysis of eMI substrates in WT and L2AKO mice distributed them into five categories: proteins with unchanged degradation (i), proteins degraded less (ii) or no longer degraded (iii) in L2AKO LE/MVBs, and proteins degraded more (iv) or only degraded (v) in L2AAKO LE/MVBs (Figure 2C). Proteins rerouted from CMA to eMI in L2AKO mice should be in categories (iv) and (v) and contain KFERQ-like motifs. Analysis of these motifs revealed enrichment in acetylation-generated motifs in the proteins potentially rerouted from CMA (Figure 2D), suggesting that acetylated KFERQ motifs may serve as a marker for cargo rerouting between CMA and eMI. The intracellular subproteome rerouted to eMI included categories of proteins not degraded in WT LE/MVBs, such as proteins related to the endoplasmic reticulum (ER) stress response and insertion of tail-anchored proteins into the ER membrane (Figure 2B, bottom), and among the top KEGG pathways were protein translation and processing in the ER (including synthesis, folding, trafficking, and membrane insertion) and lipid metabolism (cholesterol and steroids) (Figures 2E–2G and S3F).

As a second approach to identify substrate proteins rerouted to eMI from CMA, we compared the proteomes of LE/MVBs and lysosomes from livers of WT and L2AKO mice injected or not with leupeptin[34] (Figure S3G). Of 1,052 proteins degraded in lysosomes, 483 were CMA substrates (degraded in a LAMP-2A-dependent manner) (Figure S3G), and of those, only 75 were also among the 978 KFERQ-bearing proteins normally degraded by eMI. These results suggest that, although both eMI and CMA can degrade the same

proteins (Figures 1A–1C), only 7.6% of eMI substrates are simultaneously degraded by both pathways. Substrates shared between both pathways included proteins involved in different steps of translation (initiation, elongation, and termination) and metabolism of proteins (Figure S3H). Once CMA is blocked (L2AKO mice), the amount of CMA substrates undergoing degradation in LE/MVBs reached 18% (Figure S3G) and, in addition to proteins involved in protein translation (ribosome), included two new pathways related to protein processing in the ER and retinol metabolism (Figures S3I and S3J). In support of rerouting from CMA to eMI being a selective process, we did not find a correlation between rerouted proteins and their cellular abundance (Figures S3K and S3L).

Overall, our findings support the idea that CMA blockage results in changes in the intracellular subproteome degraded by eMI and possible eMI handling of CMA-regulated processes such as protein translation/folding[35] and ER protein localization and processing.

Identification of the LE/MVB proteome related to eMI activity

We sought to understand how upregulation of eMI upon CMA blockage occurs. Cellular (Figure S4A) and LE/MVB (Figures 3A and 3B) levels of known eMI components, including Hsc70 and ESCRT proteins (Vps4, Tsg101, and Alix), were comparable in WT and L2AKO mice. Of the 368 proteins identified in the LE-resident proteome (LE/MVB proteins whose levels did not increase with leupeptin), only 40 proteins differed significantly ($p < 0.05$) between WT and L2AKO LE/MVBs (Figures 3C, S4B, and S4C). Ten proteins with higher levels in L2AKO were related to peroxisomes, likely secondary to increased peroxisome number in L2AKO mice.[25] Other changing proteins included adaptor proteins, several LE/MVB proteins, cytoskeleton anchoring proteins, and proteins related to mRNA processing and protein translation (Figures S4B and S4C). We also detected 12 proteins normally stable in WT LE/MVBs that were degraded in L2AKO LE/MVBs (Figure S4B).

Since CMA blockage resulted in discrete changes only in the LE/MVB-resident proteome, in our search for eMI modulators, we first analyzed those with a reported functional relationship with Hsc70 and a known role in protein transport (Ap2a2 and Cd74)[36,37] (Figure S4D). However, CRISPR interference knockdown of Ap2a2 or Cd74 did not affect eMI activity (Figure S4E; Hsc70 [HSPA8] was used as positive control). Next, we focused on chaperones because of their role in autophagy cargo targeting. Analysis of a panel of chaperones and co-chaperones revealed higher content of most chaperones in CMA^+ lysosomes than in LE/MVBs and a further increase upon CMA activation by starvation (Figure 3D). As reported, the inducible form of Hsp70 was not present in these compartments, but we detected chaperones known to mediate substrate uptake by CMA, such as Hsc70, Hsp90, Hip, Hop, Hsp40, and CHIP.[14,38–40] Since most of them were also present at lower levels in LE/MVBs and their levels did not change upon CMA blockage (Figure 3E shows representative examples), we next analyzed Hsc70-interacting proteins in LE/MVBs, CMA^+ lysosomes, and cytosol (Figure 3F). Proteins bound to Hsc70 in cytosol and LE/MVBs or in cytosol and CMA^+ lysosomes were considered eMI or CMA substrates, respectively.

Mass spectrometry analysis of the Hsc70 pull-downs identified 125 proteins in LE/MVBs, 94 in cytosol, and 22 in CMA^+ lysosomes (Figure 3G and Table S1) and the expected

enrichment in KFERQ-like-motif-containing proteins in LE/MVBs and CMA$^+$ lysosomes (Figure 3H). Proteins targeted to CMA contained motifs generated through post-translational modification (phosphorylation and acetylation) with higher frequency than eMI substrates (Figure 3H). Interestingly, less than 5% of LE-Hsc70-associated proteins were also detected bound to Lys-Hsc70 (Figure 3G), supporting preferential targeting of substrates to these pathways. The different functional categories of Hsc70-bound cargo in LE/MVBs and CMA$^+$ lysosomes (Figures S5A and S5B) further emphasized that these autophagic processes are not redundant and each degrades a specific subset of the cellular proteome.

Bag6 was the chaperone in the Hsc70 pull-downs (Figure 3I) that fulfilled the most requirements as a possible eMI regulator: (1) it interacted only with Hsc70 in LE/MVBs, (2) it was not degraded in LE/MVBs basally, (3) STRING analysis demonstrated Bag6 functional interaction with six proteins changing in LE/MVBs upon CMA blockage (Figures S4B, highlighted in yellow, and S4F), and (4) it contributes to quality control of newly synthesized nascent proteins and of ER tail-anchored type II transmembrane proteins,[41,42] which were among those degraded more in LE/MVBs upon CMA blockage (Figures 2E–2G, S3I, and S3J). Immunoblot demonstrated Bag6 in LE/MVBs and CMA$^+$ lysosomes, but not in macro-autophagy-engaged lysosomes (CMA$^-$)[43] (Figure S5C) and pulldown confirmed Bag6/Hsc70 interaction in LE/MVBs (Figure S5D).

Bag6 contributes to regulation of eMI activity

To test if Bag6 regulates eMI, we knocked down Bag6 in mouse NIH3T3 fibroblasts stably expressing the KFERQ-Split Venus reporter using short hairpin RNA (shRNA) (Figure S5E) and small interfering RNA (siRNA) (Figure S5F). Bag6(−) cells displayed defective eMI internalization/degradation, detected as a reduced increase in fluorescent puncta upon inhibition of LE/MVB proteases with ammonium chloride/leupeptin (+N/L) (Figures 4A–4C). Although Bag6 associates with CMA$^+$ lysosomes (Figure S5C), Bag6(−) cells were still fully competent for CMA, which was significantly upregulated (Figures 4D–4F). Basal CMA upregulation was likely responsible for the higher rates of intracellular proteolysis in Bag6(−) cells (Figures 4G and 4H).

To elucidate the role of Bag6 in eMI and CMA crosstalk, we performed single- and double-knockdown experiments in cells expressing the fluorescent reporters. Compared with Vps4 knockdown, which completely blocked eMI, Bag6 knockdown resulted in a lesser decrease in eMI, with 45% of eMI being independent of Bag6 (Figure 4I). The absence of Bag6 completely abolished the upregulation of eMI observed upon CMA blockage (Figures 4I and 4J, left), while double knockdown of Vps4 and LAMP-2A still resulted in eMI upregulation, albeit small, due to the remaining levels of Vps4 (Figures 4I and 4J, right). These findings support Bag6 as a key mediator of the crosstalk between eMI and CMA. In fact, Bag6 knockdown induced higher upregulation of CMA than observed upon Vps4 knockdown (Figure 4K). As expected, LAMP-2A knockdown inhibited CMA upregulation in both cases (Figure 4L). To our surprise, double knockdown of Vps4 and Bag6, rather than being additive, abolished the CMA upregulation observed with the single knockdowns (Figure 4K), suggesting that the presence or absence of Bag6 may be relevant only for rerouting of substrates from eMI to CMA in the context of a functional eMI.

Since Bag6 is required for eMI upregulation in CMA-deficient models (Figures 4I and 4J), we next investigated the underlying mechanism. CMA blockage did not change cellular or LE/MVB abundance of Bag6 (Figures S5G and S5H), and immunofluorescence in isolated LE/MVBs incubated with Tau (to identify LE/MVBs active for eMI) revealed no difference in the percentage of $Bag6^+$ LE/MVBs (Figures S5I and S5J) or of $Bag6^+$ eMI-competent LE/MVBs ($LAMP\text{-}1^+$, Tau^+ vesicles; Figures S5I and S5K) upon CMA blockage. However, blue native electrophoresis of isolated LE/MVBs immunoblotted for Bag6 demonstrated higher abundance of Bag6 in high-molecular-weight protein complexes in LE/MVBs from CMA-deficient animals (Figure 4M). Bag6-positive complexes in LE/MVBs did not co-migrate with Hsc70, but showed some overlap with the ESCRT-associated protein Alix, which has a known role in eMI (Figure 4M). We propose that eMI upregulation upon CMA blockage may be due, at least in part, to increased engagement of Bag6 in eMI-related complexes.

To identify the subproteome degraded by eMI in a Bag6-dependent manner, we compared the proteome of LE/MVBs isolated from control and Bag6(−) cells using stable isotope labeling by amino acids in cell culture (SILAC) and quantitative proteomics. About half of the proteins normally detected in LE/MVBs were absent in this compartment in Bag6(−) cells (Figure 4N and Table S2). The pool of proteins still detected in Bag6(−) LE/MVBs (Bag6 independent; n = 376) showed less abundance of KFERQ-containing proteins than those no longer detected (Bag6 dependent; n = 354) (Figure 4O). Comparison with the list of intracellular proteins identified as putative eMI substrates (Figure 2B) revealed that of the 268 eMI substrates detected in WT LE/MVBs, 40% were no longer detected in LE/MVBs from Bag6(−) cells (Figure 4P). We did not find a correlation between cellular levels and dependence on Bag6 (Figures S5L and S5M). STRING analysis demonstrated enrichment in the Bag6-dependent group of proteins involved in carbon metabolism and cytoskeleton organization, but the most noticeable enrichment was for proteins involved in “protein processing in the ER,” followed by intracellular protein metabolism (Figures 4Q and 4R), which coincides with those enriched in proteins rerouted to eMI upon CMA blockage (Figures S3I and S3J).

Our findings confirm that Bag6 is required for eMI degradation of a specific subset of proteins and is important for rerouting of CMA substrates to eMI upon CMA blockage.

Mechanism of Bag6 regulation of eMI

Upon incubation of isolated LE/MVBs and CMA^+ lysosomes, we found that Bag6 is stable in LE/MVBs but undergoes gradual degradation in CMA^+ lysosomes (Figures 5A and 5B). Trypsinization of isolated organelles to digest proteins on the cytoplasmic surface of the membrane (mTOR), but not luminal proteins (GBA) (Figures 5C and 5D) revealed that most of the Bag6 was on the cytosolic side of the LE/MVB and lysosome limiting membranes, although a small fraction of LE/MVB-associated Bag6 was resistant to trypsin, in support of some internalization (Figures 5C and 5D).

We next preincubated LE/MVBs and CMA^+ lysosomes with an antibody against Bag6 to analyze the effect of this chaperone on substrate binding and internalization. Blockage of LE/MVB-Bag6 resulted in a reduction in the internalization/degradation of KFERQ-

containing substrates (GAPDH, α-synuclein, and Tau) but not of in-bulk eMI of Cyclophilin A (Figures 5E and 5F; antibody binding to the organelle is shown in Figure S6A). Bag6 has been reported to interact with Tsg101, one of the ESCRT proteins essential for eMI,[44] and we found that this interaction occurs in part in LE/MVBs, as both proteins were present in the co-immunoprecipitation of LE/MVB-Hsc70 (Figure S5E), further supporting association of Bag6 with eMI machinery.

Despite increased CMA activity in Bag6-deficient cells (Figure 4C), preincubation of lysosomes with anti-Bag6 did not affect binding or internalization of any tested CMA substrate (Figures S6B–S6D). Thus, upregulation of CMA in Bag6(−) cells is not due to a direct effect of Bag6 in lysosomes, but rather a compensatory response to eMI malfunctioning. Furthermore, proteomic studies of CMA^+ lysosomes from leupeptin-injected mice[34] revealed degradation of Bag6 in lysosomes in a LAMP-2A-dependent manner (Figure S6E), supporting the idea that Bag6 may be a lysosomal substrate.

To characterize the interplay between Bag6 and eMI components and substrates, we imaged isolated LE/MVBs upon incubation with Tau to activate eMI using super-resolution stimulated emission depletion (Tau-STED) microscopy. In contrast to the near-uniform intensity of Hsc70 signal throughout the LE/MVB membrane (Figure 5G), the Bag6 signal appeared as discrete foci along the membrane (Figure 5H). We used tracing of the external and internal edges of LAMP-1 fluorescence in each LE/MVB and defined the space in between the two as the LE/MVB membrane and that inside the inner trace as the lumen (Figure S6F). Then we calculated the fluorescence intensity for each protein in the LE/MVB perimeter relative to the total signal in the membrane to account for differences in antibody affinity. Areas of high signal for Hsc70 and Bag6 or “hotspots” (pixels with intensity >1.25 times the average total membrane signal) overlapped with those of high Tau signal (41.3% and 50.8% for Hsc70 and for Bag6, respectively; Figure S6G), suggesting that the two chaperones are normally found in LE/MVB membranes in close proximity with the substrate. While hotspots containing both Hsc70 and Tau were detected throughout the membrane (Figure 5G, right), hotspots for Bag6 were more commonly found flanking substrate hotspots (Figure 5H, right). As Bag6 is required for substrate internalization, these could be areas of intraluminal vesicle formation.

Analysis of the distribution of Bag6 and Hsc70 revealed that luminal content of Hsc70 and Bag6 per vesicle highly correlates with the fraction of Tau detected in their lumen (Figure 5I). Tau-STED microscopy in LE/MVBs incubated with or without Tau revealed that addition of substrate did not change the membrane pattern of distribution of Bag6 and Hsc70 (which remained diffuse for Hsc70 and focal for Bag6), but promoted higher coincidence of both chaperones in the same membrane hotspot (Figure 5J) and higher levels of Bag6 and Hsc70 in the LE/MVB lumen (Figure 5K). These findings suggest that a fraction of both chaperones is internalized with the substrate during eMI and reinforce involvement of Bag6 in substrate internalization.

Starvation reduces eMI activity and LE/MVB-associated Bag6

Macroautophagy and CMA mediate turnover of proteins during nutrient deprivation[21,45]; however, the impact of nutrients on mammalian eMI remains unknown. We found

significantly reduced Tau binding and internalization in LE/MVBs isolated from 24-h-starved rodents compared with *ad libitum*-fed rodents (Figures 6A and 6B) and that this decrease was gradual during the course of starvation (Figures 6C and 6D). We attributed the discrete, but consistent, increase in Tau internalization/degradation at 6 h of starvation to the previously reported early starvation induction of in-bulk eMI.[46] The inhibitory effect of starvation preferentially affects selective eMI, as binding and internalization/degradation of Cyclophilin A were comparable in LE/MVBs from fed and starved animals (Figures 6A and 6B). We confirmed the effect of starvation on eMI *in vivo* using LE/MVBs from livers of fed and 24-h-starved animals injected with leupeptin (positive controls for leupeptin shown in Figure S7A). Several endogenous KFERQ-containing substrates (LRRK2, Hexokinase, and Aldolase) exhibited consistently reduced degradation in LE/MVBs from starved animals, whereas degradation of Cyclophilin A remained unchanged (Figures 6E and 6F). Interestingly, the effect of starvation seems specific even among KFERQ-bearing proteins, since eMI degradation of GAPDH was comparable between fed and starved animals both endogenously (Figures 6E and 6F) and using the *in vitro* reconstitution assay (Figures 6C and 6D).

Immunofluorescence of LE/MVBs isolated from fed and 24-h-starved rats after incubation with Tau revealed no changes with starvation in the percentage of LE/MVBs capable of performing eMI (LAMP-1$^+$/Tau$^+$ vesicles) (Figure 6G), supporting the idea that the decrease in eMI capacity is per LE/MVB and likely due to intrinsic changes in these organelles during starvation. We did not find differences in the degradation of a pool of radiolabeled proteins between LE/MVBs isolated from fed and 24-h-starved animals once their membranes were disrupted (Figure 6H), suggesting that reduced eMI with starvation is at the level of substrate binding/internalization. Analysis of LE/MVBs isolated from fed and 24-h-starved rat livers revealed no differences in their enzymatic activity (Figure S7B); levels of markers such as LAMP-1, GBA, or Rab7 (Figures 7A and 7B); or known eMI effectors such as ESCRT proteins (Vps4 and Alix) or Hsc70 (Figures 7A and 7B). However, we noticed a significant 57% reduction in levels of Bag6 in LE/MVBs from starved animals (Figures 7A and 7B), which was not due to reduced cellular Bag6 levels (Figures S7C and S7D) and was specific for Bag6 among LE/MVB chaperones (Figures 7C and 7D). Starvation did not change the interactions of Hsc70, Bag6, and Tsg101 in LE/MVBs (Figure S5E), in support of the idea that the Bag6 present in these organelles was still functional and that eMI decline was mostly due to an overall decrease in Bag6 in this compartment.

Tau-STED microscopy of isolated LE/MVBs revealed no changes upon starvation in the membrane distribution of Hsc70 and Bag6, but we noticed significantly higher levels of both chaperones in the LE/MVB lumen (Figures 7E, 7F, S7E, and S7F). Incubation of LE/MVBs with the substrate Tau no longer elicited the internalization of Hsc70 and Bag6 observed in fed LE/MVBs (Figure 7F). In fact, we confirmed that the substrate-driven internalization of Bag6 relative to Hsc70 in LE/MVBs from fed animals was no longer noticeable in LE/MVBs from starved animals (Figures 7G and 7H). These results support the idea that higher luminal content of Bag6 and Hsc70 in starved animals is not a consequence of increased substrate internalization, but rather a substrate-independent event that may contribute to reduced eMI activity by limiting accessibility of substrates to eMI chaperones.

We propose two possible non-exclusive mechanisms behind lower Bag6 levels in LE/MVBs: (1) reduced targeting of Bag6 to LE/MVBs and/or (2) release or degradation of the subset of Bag6 engaged in eMI. Analysis of Bag6 isoelectric pattern using bidimensional electrophoresis revealed that starvation resulted in a shift of several cytosolic Bag6 isoforms toward a more acidic pH, in support of possible phosphorylation (Figure S7G). Bag6 has several KFERQ-like motifs in its sequence, including three that can be generated through phosphorylation of an incomplete motif (Figure S7G, inset). It is possible that the fraction of Bag6 normally engaged in eMI could undergo phosphorylation and subsequent targeting for lysosomal degradation. In support of this possibility, Bag6 accumulates in lysosomes isolated from leupeptin-injected WT mice, but not from L2AKO mice (Figure S6E).

Overall, our findings highlight Bag6 as an eMI component and regulator of the coordinated function of eMI and CMA, illustrated here through their opposing responses to starvation.

DISCUSSION

This work provides evidence of crosstalk between CMA and eMI, two selective autophagy pathways that share a chaperone and substrate-targeting motif.[18,47] We demonstrate that although a subset of the KFERQ-containing proteome undergoes degradation by each of these pathways, the same protein can be degraded by either pathway, albeit with different efficiencies. Tau is the only protein identified so far to undergo degradation in LE/MVBs as efficiently as in lysosomes. It is possible that Tau aggregation triggered by its high local concentration inside intraluminal LE/MVB vesicles[48] leads to vesicle rupture and exposure to endosomal proteases. The versatility of the degradation of KFERQ-containing proteins allows for rerouting of CMA cargo to eMI when CMA is blocked. We have also identified an inverse switch in their activities upon nutrient restriction, whereby starvation inhibits eMI and stimulates CMA. Starvation-induced changes in endosomal abundance and topology of Bag6 are likely behind the decline of eMI.

Rerouting of CMA substrate proteins to eMI upon CMA blockage may have relevance in disease contexts where CMA activity is compromised, such as Alzheimer's[27] and Parkinson's diseases.[49,50] Pathogenic proteins unable to undergo CMA degradation could instead be rerouted to degradation through eMI, as recently shown for mutant forms of Tau.[20] Rerouting of pathogenic toxic proteins will prevent their intracellular accumulation, but rerouting of functional proteins degraded for regulatory purposes may still result in cellular impairments because their function is prolonged, since the time at which they are degraded is different. For example, upon CMA failure, delayed degradation of clock machinery components leads to alterations in circadian rhythm,[34] and delayed CMA degradation of transcription factors during adipocyte differentiation leads to defective adipogenesis.[51]

In this study, we have performed analyses in both cultured cells and rodent liver tissue as both provide unique advantages. Cultured cells allow for (1) tracking eMI and CMA with fluorescent reporters and (2) performing genetic manipulations. Liver tissue (1) provides a large amount of starting material for organelle isolation and (2) is a fairly homogeneous

tissue (hepatocytes are 80% of the liver mass)[52]; (3) hepatic CMA and eMI have been well characterized[25,53] and (4) liver tissue allows for the study of physiological responses *in vivo*.

The opposite responses of eMI and CMA to starvation suggest a more active role for eMI in maintenance and regulation of the cellular proteome under basal conditions and a lesser contribution to cellular energetics during starvation. Reduced eMI during starvation may represent a coordinated cellular effort to recycle un-needed proteins (as a source of free amino acids) while preserving those that are essential to surviving starvation. It is possible that CMA degrades KFERQ-containing proteins that are expendable and eMI degrades proteins involved in cellular survival of starvation. The inhibition of KFERQ-mediated eMI during starvation adds to its differences with other types of microautophagy, such as the Hsc70-independent but ESCRT-dependent form of eMI activated in the early phase of starvation.[46,54] Similarly, the starvation-dependent inhibition of mammalian eMI is in contrast with the increase in eMI during starvation identified in *Drosophila*.[55,56] It is possible that since invertebrates lack CMA, eMI may fill some of the functions reserved for CMA in mammals.

This work adds the involvement of Bag6 in eMI to the multiplicity of functions already described for this ubiquitous cellular protein.[41] Bag6 interacts with the ESCRT proteins Alix and Tsg101[44,57] to facilitate loading of exosomes.[44] Since (1) both ESCRT proteins are required for eMI,[18] (2) the Bag6/Tsg101 interaction occurs in LE/MVBs through Hsc70, (3) depletion of Bag6 results in changes in the substrate proteins undergoing degradation in LE/MVBs, and (4) LE/MVBs are compartments shared between eMI and exosome biogenesis,[58] loading of eMI substrates via the interaction of Bag6/ESCRT proteins is an attractive mechanism for the role of Bag6 in eMI. The proteins delivered to LE/MVBs in a Bag6-dependent manner relate well with the described role of Bag6 in ER and protein translation quality control,[41] although so far only their proteasome targeting had been reported.

The specific role of the interaction of Bag6/Hsc70 in the context of eMI will require further study, but we propose that it may be essential for cargo sorting and favor a model in which Bag6 will have a dual function in LE/MVBs as a cargo “holdase”−to keep partially unfolded substrate proteins soluble− and also as a trigger for substrate loading into the vesicles through its interaction with the ESCRT machinery.

Given the variety of Bag6 cellular functions, it is likely that post-translational modifications allocate a subset of Bag6 to each of these functions. This work highlights changes in the isoelectric point of cytosolic Bag6 during starvation, compatible with phosphorylation, that may mediate degradation by CMA of only the portion of Bag6 utilized for eMI, having little impact on the total cellular pool of Bag6.

The coordinated functioning of eMI and CMA identified in this work, their inverse regulation by nutrients, and the interplay of Bag6 with both autophagic pathways provide key information on the regulation of eMI, its physiological role, and consequences of its malfunctioning.

Limitations of the study

A limitation of working with rodent models is animal-to-animal variability, which we partially overcame by performing some studies *in vivo* and in cell culture. We are also limited by the difficulty in separating eMI substrate internalization from degradation, which in the *in vitro* models we can overcome by comparing changes in proteolysis after disrupting LE/MVB membranes. However, *in vivo*, even upon injection of leupeptin prior to LE/MVB isolation, we will miss substrates internalized in LE/MVBs by eMI but degraded only upon lysosome fusion.

The fate of cellular KFERQ-containing proteins when CMA and eMI are both blocked is currently difficult to monitor because of the severe impact of double knockdown on cell proliferation, making isolation of organelles unfeasible. Tracking changes in substrate protein levels is not informative because they do not always increase due to rerouting to other proteolytic systems or extracellular release.

STAR★METHODS

RESOURCE AVAILABILITY

Lead contact—Further information and requests for reagents may be directed to and will be fulfilled by the co-corresponding author Ana Maria Cuervo (ana-maria.cuervo@einsteinmed.edu).

Materials availability—All reagents generated in this study are available from the lead contact with a completed Material Transfer Agreement.

Data and code availability

- There are no restrictions on data availability in this manuscript. All Main and Supplementary Figures have associated raw data that is provided as an Excel worksheet organized by figures and includes statistics along with exact p-values. The raw data of the proteomic analysis of LE/MVBs (including the WT and L2A KO comparative proteomics and the WT and Bag6 KD comparative proteomics) and from the Hsc70 IP have been deposited to the ProteomeXchange Consortium[64] (http://proteomecentral.proteomexchange.org) via the PRIDE partner repository with dataset identifiers PXD029580, PXD046760 and PXD046797.
- This paper does not report original code.
- Any additional information required to reanalyze the data reported in this paper is available from the lead contact upon request.

EXPERIMENTAL MODEL AND STUDY PARTICIPANT DETAILS

Animal models—Adult (3–6 months) male Wistar rats (Charles River Laboratories) were used in this study, in addition to adult (3–6 months) male mice (C57BL/6J) wild-type mice or systemically knockout for LAMP-2A (L2AKO; generated by insemination of a wild-type female with spermatozoids with L2A floxed to excise this gene in all tissues

in the offspring[25]). All mice were in the C57BL/6J background and maintained under specific pathogen-free conditions in ventilated cages with no more than 5 mice per cage. All rats were in the Wistar background maintained under specific pathogen-free conditions in ventilated cages with no more than 2 rats per cage. Only males were used in this study due to the difficulty in achieving meaningful sample size in both males and females in the experiments utilizing isolated subcellular compartments. Animals were maintained at 19–23°C in a 12h light/dark cycle and fed *ad libitum,* except where indicated. Rodents deprived of food were given *ad libitum* access to water. To study LE/MVB protein degradation *in vivo*, rodents were injected i.p. with a single dose of leupeptin (Sigma L5793; 40mg/kg b.w. in saline (0.9% NaCl)) or with saline only and tissues were collected 4h after injection. Animals were randomly assigned to the leupeptin or saline injection group. All animal genotyping, breeding, handling and treatments in this study were done according to protocol and all animal studies were under an animal study protocol approved by the Institutional Animal Care and Use Committee of the Albert Einstein College of Medicine.

Cell culture and treatments—NIH3T3 mouse fibroblasts from the American Type Culture Collection (ATCC) were maintained in DMEM (Sigma-Aldrich) in the presence of 10% newborn calf serum (NCS) (Atlanta Biologicals) and 1% penicillin/streptomycin/fungizone (Invitrogen) in a 37°C incubator with 5% CO_2. For eMI flux assays, cells were treated with lysosomal inhibitors ammonium chloride (20μM, American Bioanalytical) and leupeptin (100μM, Fisher Scientific) for the indicated time. Information on shRNA and siRNA oligonucleotides are in the key resources table. CRISPRi of Hsc70, CD74 and Ap2a2 was performed using a pool of 5 sgRNAs introduced by lentiviral delivery.[65] Cells were transfected with Lipofectamine RNAiMAX transfection Reagent (Life Technologies) in Opti-MEM media without antibiotics. Cell lines were routinely tested for mycoplasma contamination using DNA staining protocol with Hoechst 33342 (Invitrogen, H3570).

METHOD DETAILS

Reagents—Sources of chemicals are found in the key resources table

Antibodies—The dilutions and sources of antibodies used for immunoblot (IB), immunoprecipitation (IP), cell immunofluorescence (cell-IF) and isolated LE/MVB immunofluorescence (LE-IF) in this study were as follows: (dilutions, commercial source, and catalog number indicated in parentheses): rabbit anti-aldolase (1:1000 (IB), Cell Signaling, 3188S), rabbit anti-Alix (1:500 (IB), Novus, NBP1–90201), mouse anti-Alix (3A9) (1:100 (LE-IF), Cell Signaling, 2171S), mouse anti-α synuclein (211) (1:2000 (IB), Santa Cruz, sc-12767), rabbit anti-ATP6V1B (1:1000 (IB), Abcam, ab200839), rabbit anti-Bag1 (1:1000 (IB), Abcam, ab32109), rabbit anti-Bag3 (1:1000 (IB), Novus, NBP2–27398SS), sheep anti-Bag6 (1:200 (IB) and 1:100 (LE-IF), R&D Systems, AF6438), rabbit anti-Bag6 (1:1000 (IB), 1:100 (LE-IF), 1μg (IP), Abcam, ab137076). rabbit anti-Cathepsin B (1:1000 (IB), Abcam, ab214428), mouse anti-cathepsin D (D-7) (1:500 (IB), Santa Cruz, sc-377299), rabbit anti-cathepsin L (H-80) (1:1000 (IB), Santa Cruz, sc-10778), rabbit anti-CHIP (C3B6) (1:1000 (IB), Cell Signaling, 2080), rabbit anti-Cyclophilin A (1:1000 (IB), Cell Signaling, 2175), mouse anti-EEA1 (1:1000 (IB), BD Biosciences, 610456, RRID AB_397830), rabbit anti-GAPDH (1:2000 (IB), Cell Signaling, 2118S), rabbit anti-

GBA (1:1000 (IB), Sigma, G4171), rabbit anti-hexokinase (1:1000 (IB), Cell Signaling, 2024S), rabbit anti-HIP (1:1000 (IB), Stressgen, adi-spa-766), rabbit anti-HOP (1:1000 (IB), Enzo, adi-sra-1500), mouse IgM anti-Hsc70 (13D3) (1:3000 (IB) and 1:200 (LE-IF), Novus, nb120–2788), rabbit anti-hsp40 (1:1000 (IB), Assay Designs, adi-spa-410), rabbit anti-hsp90 (1:1000 (IB), Stressgen, ADI-SPA-835-F), rat anti-LAMP-1 (1D4B) (1:3000 (IB) 1:200 (LE-IF) 1:2000 (Cell-IF), Hybridoma Bank, 1D4B, RRID AB_2134500), mouse-anti LAMP-1 (LyC16) (1:1000 (IB) and 1:100 (LE-IF), Enzo, adi-vam-en001), rabbit anti-LAMP-2A (1:5000 (IB), ThermoFisher Scientific, 512200, RRID AB_2533900) rabbit anti-LC3 (1:1000 (IB), Cell Signaling, 2775, RRID AB_915950), rabbit anti-LRRK2 (MJFF3) (1:1000 (IB), Abcam, ab133475), rabbit anti-mTOR (1:2000 (IB), Cell Signaling, 2972), mouse anti-p62 (1:1000 (IB), Abcam, ab56416), rabbit anti-Rab7 (D95F2) (1:500 (IB), Cell Signaling, 9367), mouse anti-total Tau (DA9) (1:3000 (IB) and 1:200 (LE-IF), gift from Dr. Peter Davies), rabbit anti-Tsg101 (1:1000 (IB) and 1:100 (LE-IF), Abcam, ab30871), mouse anti-tubulin (1:1000 (IB), Sigma, T7451), rabbit anti-ubiquitin (1:1000 for IB and for Cell-IF, Dako, Z0458, RRID AB_2315524), mouse anti-Vps4 (E-8) (1:500 (IB) and 1:100 (LE-IF), Santa Cruz, sc-133122), rabbit anti-Hsc70 (1μg (IP), Enzo, ADI-SPA-757), rabbit normal IgG (1μg (IP), Cell Signaling, 2729S). All secondary antibodies for routine immunofluorescence were from ThermoFisher Scientific. Secondary antibodies for standard emission depletion microscopy were from the following sources: goat anti-mouse 594 ATTO (1:200, Rockland, 610–155-121), goat anti-rabbit 594 ATTO (1:200, Sigma, 77671–1ML-F), goat anti-mouse 647 ATTO (1:200, Sigma, 50185–1ML-F), and goat anti-rabbit 647N ATTO (1:200, Rockland, 611–156-122). All antibodies used were validated following the multiple dilution method and, where available, using cell lines or tissues from animals knock-out for the antigen.

Isolation of subcellular compartments—Rodent liver lysosomes and LE/MVBs were isolated after tissue homogenization and centrifugation in density gradients. For lysosomes, homogenates were subjected to differential centrifugation to obtain a light mitochondrial/lysosome fraction, which was subsequently ultracentrifuged in a discontinuous metrizamide density gradient.[66] Lysosomes active (+) or inactive (−) for CMA were separated by differential centrifugation as described before[39]. LE/MVBs were isolated from rodent livers through consecutive discontinuous density gradients of sucrose and Percoll (GE Healthcare) as described previously.[18,67] Endolysosomal compartment integrity after isolation was assessed by measuring enzymatic β-hexosaminidase activity released from the pelleted organelles.[68] Only isolations with less than 10% membrane breakage were used for subsequent analyses. Cytosol was obtained by centrifugation at 100000xg for one hour of the post-nuclear supernatant. Except for the transport studies, all fractions were supplemented with protease inhibitor (10mM leupeptin, 10mM 4-(2-aminoethyl) benzenesulfonyl fluoride hydrochloride, 1mM pepstatin, 100mM EDTA) and phosphatase inhibitor cocktails 2 (Sigma P5726) and 3 (Sigma P0044) prior to freezing.

Autophagy measurements in isolated organelles—*Lysosomal and LE/MVB binding and uptake* of substrate proteins were analyzed using a previously described *in vitro* system.[22,67] Briefly, lysosomes or LE/MVBs were preincubated or not with a cocktail of protease inhibitors for 10 min on ice and then incubated with recombinant proteins

(Tau (rPeptide, T-1001–2), LRRK2 (ThermoFisher Scientific, PV4873), GAPDH (Sigma, G2267), Cyclophilin A (R&D systems, 3589-CA-100), or α-synuclein (rPeptide, S-1001–2)) in MOPS-Sucrose buffer (20mM MOPS, 0.3M sucrose, pH 7.3) at 37°C for 20 min (lysosomes)[22] or 30 min (LE/MVBs).[67] At the end of the incubation, lysosomes or LE/MVBs were collected by centrifugation, washed to remove unbound substrate and processed for SDS-PAGE and immunoblotting. Binding was calculated as the amount of protein associated with organelles untreated with protease inhibitors and internalization/degradation as the difference between proteins present in organelles treated with protease inhibitors after subtracting for the amount bound. *Proteolysis* in isolated LE/MVBs was assayed by incubating them with a pool of radiolabeled proteins in 20mM MOPS, 0.3M sucrose, 1mM DTT and 5.4μM cysteine pH 7.3. This assay was performed in intact LE/MVBs or while incubating with 0.2% Triton-X100 (BioRad) to rupture the LE/MVB membrane and release the luminal proteases.

Autophagy measurements in cultured cells—*eMI activity* was measured in cells stably transduced with lentivirus containing the KFERQ-Split Venus reporter.[27,28] Cells were plated in glass-bottom 96-well plates and eMI flux was assessed with the addition or not of endolysosomal protease inhibitors (20mM ammonium chloride and 100μM leupeptin; +N/L in text). Atter 16 hours, cells were fixed with 4% PFA and imaged using high-content microscopy (Operetta system, Perkin Elmer) set to collect images from ≥ 800 cells/condition. *CMA activity* was measured in cells stably transduced with lentivirus carrying the KFERQ-PS-Dendra reporter[29,30] 16h hours after photoswitching with an LED lamp (405nm for 3 minutes), and *macroautophagy activity* in cells stably transduced with lentivirus containing the mCherry-GFP-LC3 reporter.[69] In both cases, cells were fixed with 4% PFA and imaged using the same high-content microscopy system as for the eMI reporter. Images were quantified using the manufacturer's software to detect fluorescent puncta, and changes in eMI and CMA activity were quantified as changes in the number of fluorescent puncta per cell. Macroautophagy flux was determined by the conversion of $mCherry^+/GFP^+$ puncta (autophagosomes) into $mCherry^+$ puncta only (autolysosomes) as a result of GFP quenching in the low pH of the lysosome. Nuclei were labeled with Hoechst.

Intracellular protein degradation—Degradation of long-lived proteins was measured in confluent cells by metabolic labeling with ^{3}H-leucine (2 μCi/ml) for 48h at 37°C. After extensive washing, cells were kept in media containing an excess of unlabeled leucine (2.8mM) to prevent the reutilization of radiolabeled leucine, supplemented with or without 10% NCS. Aliquots of media taken at different times were precipitated with TCA and proteolysis was measured as the percentage of acid-insoluble radioactivity (protein) transformed into acid-soluble radioactivity (amino acids and small peptides) at the end of the incubation. Total radioactivity incorporated into the cellular proteins was determined as the amount of acid-precipitable radioactivity in labeled cells immediately after washing. The fraction of intracellular degradation occurring in lysosomes was identified as that inhibited by N/L and degradation by macroautophagy as the fraction of lysosomal protein degradation inhibited by 3-methyl adenine.

Co-immunoprecipitation—Isolated LE/MVBs were resuspended in co-immunoprecipitation (coIP) buffer (20mM MOPS, 0.3M sucrose, 1mM DTT, 0.5% NP-40, pH 7.3) supplemented with a cocktail of protease inhibitors and incubated on ice for ten minutes before centrifugation at 16000xg for 15 minutes at 4°C. Solubilized proteins were incubated with primary antibodies for 2h under continuous rotation. Protein A/G Plus agarose beads (Santa Cruz, sc-2003) were added for an additional 1h. After extensive washing, immunoprecipitated proteins were eluted and prepared for standard SDS-PAGE and immunoblotting.

Protein topology in isolated organelles

Trypsinization assay: To assess the percentage of protein that is membrane-bound versus internalized in an organelle lumen, isolated organelles were incubated with trypsin (Sigma, Cat # T1426) in isotonic media at room temperature for 15 minutes. Triton-X100 (0.1%) was added to a control sample to confirm full degradation of organelle components by trypsin once the membrane is lysed.

Stability assay: To assess the stability of a protein in the membrane of an organelle, the organelle is incubated at 37°C for time intervals up to 30 min in 20mM MOPS, 0.3M sucrose, 1mM DTT and 5.4μM cysteine pH 7.3, with a control condition incubated with protease inhibitors to assess for degradation as the cause for stability loss during incubation. Protein stability is determined in reference to unincubated organelles. After each time point, samples are prepared for standard SDS-PAGE immunoblotting.

Protein electrophoresis and immunoblotting: Protein concentration was determined using the Lowry method[70] with bovine serum albumin as the standard. Immunoblotting was performed after transferring SDS-PAGE gels to nitrocellulose membrane and blocking with 5% milk in 0.01% Tween-TBS for 1h at room temperature. The proteins of interest were visualized after incubation with primaries by chemiluminescence using horseradish peroxidase-conjugated secondary antibodies in the LAS-3000 Imaging System (Fujifilm, Tokyo, Japan). Densitometric quantification of the membranes was performed using ImageJ (NIH;[71]). All protein quantifications were done after normalization of protein levels to a loading control (tubulin) or Ponceau S staining. When the number of experimental conditions exceeded the number of lanes available in the gel, all gels for the same experiment included one lane with the same sample, which was used to normalize samples across gels after densitometric quantification. Isoelectric focusing (IEF) was done using the Protean IEF Cell (Bio-Rad) at 20°C with rapid ramping to a voltage of 10000V at a current limit of 50μA per strip using IPG strips with a pH 4–7 range (Bio-Rad). After isoelectric focusing and equilibration with 2% SDS (American Bioanalytical), 375mM Tris-HCl (American Bioanalytical) pH 8.8, 6M Urea, 20% (v/v) glycerol (American Bioanalytical, Cat # AB00751) supplemented with 130mM DTT (American Bioanalytical, Cat # AB00490–00010) in the first wash or 135mM iodoacetamide (Sigma, Cat # 16125) in the second wash, IPG strips were subjected to SDS-PAGE electrophoresis and subsequent immunoblotting, as described above.

Blue-native electrophoresis: LE/MVB membranes were solubilized in 1% octyl glycoside diluted in 20mM MOP, 0.3M sucrose, pH 7.3 for 15 minutes on ice followed by centrifugation at 16000xg for 15 minutes. The supernatant was prepared for blue-native electrophoresis with NativePAGE Sample Prep Kit (ThermoFisher, BN2008). Electrophoresis was done using NativePAGE 3–12% Novex Bis-Tris pre-cast gels (Invitrogen, bn1001) before transferring to a PVDF membrane (Immobilon) for immunoblotting as described above.

Immunofluorescence

Cells: *Immunofluorescence* was performed on cells grown on coverslips and fixed for 20 min with 4% PFA, permeabilized and blocked with 1% BSA, 0.01% Triton X-100 in phosphate saline buffer (PBS). Incubation with primary and secondary antibodies in 0.1% BSA in PBS was performed at room temperature for 1h each, and coverslips were mounted in DAPI-Fluoromount-G (Southern Biotechnology; ThermoFisher scientific) to stain the nucleus. *LE/MVB imaging* was performed by spotting isolated LE/MVBs on a PTFE printed slide, 6mm diameter (Electron microscopy sciences) and fixing with 8% PFA for 15 minutes. Permeabilization was performed with 0.1% glycine, 2% fetal bovine serum, 1% BSA, with 0.01% Triton X-100, after which LE/MVBs were incubated with primary and secondary antibodies at the described concentrations for 10 min each at room temperature. Mounting was performed with ProLong Diamond Anti-Fade Mountant (ThermoFisher Scientific). Confocal images were acquired with a Leica TCS SP8 (Leica Microsystem) with a 63x objective and a 1.4 numerical aperture. All images were prepared using the LASX software (Leica Microsystem) and analyzed with ImageJ (NIH) software.[71] The colocalization plugin in ImageJ was used to determine the percentage of co-localization after the thresholding of individual images.

LE/MVB imaging was performed by spotting isolated LE/MVBs on a PTFE printed slide, 6mm diameter (Electron microscopy sciences) and fixing with 8% PFA for 15 minutes. Permeabilization was performed with 0.1% glycine, 2% fetal bovine serum, 1% BSA, with 0.01% Triton X-100, after which LE/MVBs were incubated with primary and secondary antibodies at the described concentrations for 10 min each at room temperature. Mounting was performed with ProLong Diamond Anti-Fade Mountant (ThermoFisher Scientific). Confocal images were acquired with a Leica TCS SP8 (Leica Microsystem) with a 63x objective and a 1.4 numerical aperture. All images were prepared using the LASX software (Leica Microsystem) and analyzed with ImageJ (NIH) software.[71] The colocalization plugin in ImageJ was used to determine the percentage of co-localization after the thresholding of individual images.

Tau-STED imaging: Samples were imaged on a Leica TCS SP8 STED 3X outfitted with a Tau-STED module. The system was equipped with a White Light Laser and a STED pulsed laser 775nm, using a Leica HC Plan-Apo 100x/1.4 NA Oil lens. 1024×1024-pixel images were acquired at 200 Hz using HyD detectors. Samples were illuminated with the white light laser at 488, 594, and 647 nm wavelengths with the following parameters based on primary and secondary antibody staining: 1) *Alexa Fluor 488* acquisition parameters were: 6%−10% (excitation laser strength), 500–570nm (emission wavelength range), 454 (gain),

line repetition of 3, frame repetition of 4. 2) *anti-mouse IgM Atto594* acquisition parameters were: 1.5–3% (excitation laser strength), 610–630nm (emission wavelength range), 364 (gain), line and frame repetition of 2, with the 775nm STED pulsed laser at 50%. Tau-STED parameters of 130 (Tau strength) and 0.3–10.9ns (time gating) were used. 3) *anti-mouse IgG Atto647 (Tau DA9 primary antibody)* acquisition parameters were: 8% (excitation laser strength), 659–749 nm (emission wavelength range), 418 (gain), line repetition of 3, frame repetition of 4, with the 775nm STED pulsed laser at 50%. Tau-STED parameters were 50 (Tau strength) and 0.2–10.6ns (time gating). 4) *anti-rabbit IgG Atto647N (Tau Y9 primary antibody)* acquisition parameters were: 8% (excitation laser strength), 659–749 nm (emission wavelength range), 463 (gain), line and frame repetition of 4, with the 775nm STED pulsed laser at 50%. Tau-STED parameters were: 30 (Tau strength) and 0.1–10ns (time gating). 5) *anti-rabbit IgG Atto647N (Bag6 primary antibody)* acquisition parameters were: 8–20% (excitation laser strength), 659–749 nm (emission wavelength range), 364 (gain), line and frame repetition of 2, with the 775nm STED pulsed laser at 60%. Tau-STED parameters were 100 (Tau strength) and 0.2–11.1ns (time gating). 6) *anti-rabbit IgG Atto594 (Bag6 primary antibody)* acquisition parameters were: 20% (excitation laser strength), 610–630nm (emission wavelength range), 304 (gain), line and frame repetition of 4, with the 775nm STED pulsed laser at 50%. Tau-STED parameters were 10 (Tau strength) and 0.1–10.6ns (time gating).

For Tau-STED image analysis, images were prepared using the LASX software (Leica Microsystem) and analyzed with ImageJ (NIH) software.[71] Briefly, images were saved as individual channels and a gaussian deblur of sigma=2 was applied. The percentage of total signal in the membrane and lumen for each channel was assessed by using the LAMP-1 channel to draw a region of interest (ROI) around the whole LE/MVB and the inner portion of the membrane to select the lumen. Both ROIs were saved and applied to the other channels in the same LE/MVB. Values were calculated as the percentage of total LE/MVB signal in each region (membrane or lumen). The distribution of the signal in the LE/MVB membrane was measured by using the plot profile function in the LAMP-1 channel to trace the membrane. This ROI was then saved and applied to all channels for a given LE/MVB. Signal for each channel was normalized independently to the average signal in that channel. Signal that was greater than 1.25x the average signal was defined as a “hot spot” for that protein the LE/MVB membrane. Overlap of hot spots in different channels was defined as two or more channels having signal >1.25x the average signal for those channels in the same location in the profile around the LE/MVB membrane. Values are expressed as the percentage of total hot spots for a given channel either in reference to the LE/MVB perimeter length or the number of total hot spots for a given channel.

Electron microscopy: Cell pellets were fixed in 2.5% glutaraldehyde in 100mM sodium cacodylate, pH 7.43. Samples were post-fixed in 1% osmium tetroxide in 100mM sodium cacodylate, pH 7.43, followed by 1% uranyl acetate. After ethanol dehydration and embedding in LX112 resin (LADD Research Industries, 21210), ultrathin sections were cut on a Reichert Ultracut E and were stained with uranyl acetate followed by lead citrate. All grids were viewed on a JEOL 100CX II transmission electron microscope at 80kV.

Quantitative proteomics and protein pathway analysis: For the mass spectrometry analysis of LE/MVBs from *WT and L2AKO mice*, isolated LE/MVBs were denatured by the addition of 50uL of LYSE buffer solution from the PreOmics iST sample preparation kit, and further sample preparation was performed according to the iST kit protocol. Peptide samples were then resuspended in 4% formic acid, 3% acetonitrile and approximately 1μg of digested peptides per sample were loaded onto a 75μm ID column packed with 25cm of Reprosil C18 1.9μm, 120Å particles (Dr. Maisch GmbH HPLC, Germany) by a nanoElute high-pressure liquid chromatography system (Bruker) interfaced to the mass spectrometer via a captiveSpray source. The column was operated at 50°C, and peptides were directly eluted into a timsTOF Pro mass spectrometer (Bruker) over the course of a 50-minute acquisition by gradient elution from 4–17%B in from 0–20min, followed by an increase to 28%B from 20–40min, and then a ramp to 95%B to wash the column. The gradient was delivered by the nanoElute (Bruker), and the composition of mobile phase A and B were 0.1% formic acid in water and 0.1% formic acid in 100% acetonitrile, respectively. A data-dependent PASEF[72] acquisition method was used for data acquisition using the following parameters: 100–1700 m/z range, 0.85–1.30 V*s/cm^2 trapped ion mobility range, 1600V spray voltage, intensities of 200,000 were repeated for in PASEF 0 times, intensities of 100,000 to 200,000 were repeated for in PASEF 5 times, intensities of less than 100,000 were repeated for in PASEF 10 times, 4 PASEF MS/MS scans with a total cycle time of 0.53 s, and active exclusion for 0.4 min. All data were searched against the Uniprot mouse database (downloaded 7/2/2020). Peptide and protein identification searches were performed using the MaxQuant data analysis algorithm,[73] and all peptide and protein identifications were filtered to a 1% false-discovery rate. Label-free quantification and statistical testing was performed using the MSstats statistical R-package.[74] The Benjamini-Hochberg protocol for false discovery rate or control of false discovery rate by using fold change cutoff (|fold change| > 1.25), as previously suggested[75] were used. Relevant protein lists were ranked according to fold change compared to Ctr mice and submitted to rank-rank hypergeometric overlap test in R (v. 3.6.2)[76] using default settings.[77]

To identify proteins associated with Hsc70 in cytosol, lysosomes or LE/MVB, the fractions co-immunoprecipitated with Hsc70 were run on a 12% SDS-PAGE gel. The gel was stained with Coomassie blue and stained bands were excised and processed for MS/MS analysis following trypsin digestion. LTQ-MS/MS sequencing was performed using Nanospray LC-MS/MS on a LTQ linear ion trap mass spectrometer (LTQ, Thermo, San Jose, CA) interfaced with a TriVersa NanoMate nanoelectrospray ion source (Advion BioSciences, Ithaca, NY). MS/MS was performed using an isolation width of 2 m/z, normalized collision energy of 35% and a minimum signal intensity of 1000 counts. The sequences of each peptide were determined using the LTQ software analysis MS (mass spectroscopy) database searching with MASCOT (Mowse score above the predicted identity score) and SEQUEST (Delta Cn above 0.15, Sp200 percentage ions above 80 and Xscorr above 2) algorithms). The MS/MS scans were screened against NCBInr database as a first choice and then validated against SWISSPROT database. The search criteria included analysis of fixed chemical modifications (carbamidomethyl) and variable chemical modifications: (Tyr, Arg, Pro, Lys, Met oxidations), (deamidation of Gln and Asn). In addition, other criteria included:

trypsin missed cleavage sites (2), error for the parent molecular ion (3.2 Da) and the error for the peptide fragments (0.3 Da) were included.

Proteins differentially associated to LE/MVB of control or Bag6(−) cells were identified using Stable Isotope Labeling with Amino acids (SILAC).[78] For each sample, 50–100 μg of control (light cell or organelle lysate) and of Bag6(−) (heavy cell or organelle lysates) were mixed andtrypsin digested as described above. Eluted and desalted tryptic peptides (3–5 μg/sample) were further subjected to nanoLC/MS/MS on a Q-Exactive HF quadrupole orbitrap mass spectrometer (Thermo Fisher Scientific, Waltham, MA, USA) coupled to an Easy nLC 1000 UHPLC (Thermo Fisher Scientific) through a nanoelectrospray ion source. The mass spectrometer was operated using an already published protocol describing data–dependent acquisition (DDA) and positive ionization mode. Raw files from each technical and biological replicate were filtered, *de novo* sequenced, and assigned with protein ID using Peaks X+/Pro software (Bioinformatics Solutions) by searching against the reviewed mouse Swiss-Prot database (June 2016; 7000 reviewed entries) using the following parameters: trypsin, as restriction enzyme and two allowed missed cleaved at one or both peptide end. The parent mass tolerance was set to 20 ppm using monoisotopic mass, and fragment ion mass tolerance was set at 0.06 Da. Carbamidomethyl cysteine (+57.0215 on C) was specified in PEAKS as a fixed modification. 13C (6) Silac label (+ 6.02) and/or SILAC-2plex (R10, K6), methionine, lysine, proline, arginine, cysteine, and asparagine oxidations (+15.99 on CKMNPR), deamidation of asparagine and glutamine (NQ-0.98) and pyro-Glu from glutamine (Q-18.01 N-term) were set as variable modifications. For one given experiment, the data were validated using the false discovery rate (FDR) method built in PEAKS X, and protein identifications were accepted with a confidence score (−10lgP) >15 for peptides and (−10lgP) >15 for proteins; a minimum of one peptide per protein was allowed after data were filtered for <1.5% FDR for peptides and <2% FDR for proteins identifications ($P < 0.05$). The Scaffold Q+ (version Scaffold_5.3.0, Proteome Software Inc., Portland, OR) and PEAKS Q module (Bioinformatics solutions, Waterloo, Canada) were further used to quantitate the stable-isotopically labeled (SILAC) tryptic peptides based on the identification of feature pairs that have the same charge, similar MS1 peak area correlation over retention time, expected mass shifts caused by labeling and fall within certain mass errors. and protein identifications. In Scaffold, the peptide identifications were accepted if they could be established at greater than 94.0% probability to achieve an FDR less than 1.0% by the Scaffold Local FDR algorithm. Protein identifications were accepted if they could be established at greater than 95.0% probability to achieve an FDR less than 3.0% and contained at least 1 identified peptide. Protein probabilities were assigned by the Protein Prophet algorithm.[79] Proteins that contained similar peptides and could not be differentiated based on MS/MS analysis alone were grouped to satisfy the principles of parsimony. Normalization was performed iteratively (across samples and spectra) by subtracting the average ratios in log-space. Means were used for averaging. Spectra data were log-transformed, pruned of those matched to multiple proteins, and weighted by an adaptive intensity weighting algorithm. One average, of 14894 spectra in one given experiment at the given thresholds, 7883 (53%) were included to extract the Heavy:Light MS1 ratios which were further used to in the protein quantitation. In another independent

experiment contrasting the cytosol and LE/MVBs of Bag6(−), of 19495 spectra in the experiment at the given thresholds, 10258 (53%) were included in quantitation.

Analysis of the presence of KFERQ-like motifs was performed as previously described[31] using the publicly available tool: https://rshine.einsteinmed.org/. The mass spectrometry data from the Hsc70 pulldown experiments and SILAC in Bag6(−) cells are shown in Tables S1 and S2, respectively. The mass spectrometry data files (raw and search results) have been deposited to the ProteomeXchange Consortium[64] (http://proteomecentral.proteomexchange.org) via the PRIDE partner repository with dataset identifiers PXD029580 (WT and L2A KO LE/MVBs and cytosol) and PXD046760 (WT and Bag6 KD LE/MVBs).

QUANTIFICATION AND STATISTICAL ANALYSIS: All data presented are mean±s.e.m. Prior to statistical testing, normality was assessed using the Shapiro Wilk test. Statistical significance was compared by two-tailed unpaired Student's t-test for two groups, one-way ANOVA for a single parameter in multiple groups or two-way ANOVA for multiple parameters in multiple groups. The post hoc test used for multiple comparisons is stated in the legend of the figures. The number of animals used per experiment was calculated through power analysis based on previous results. Statistical analyses were performed either in GraphPad Prism 9.0 or using Python (Python software foundation v.3.7.4 available at https://www.python.org/) and the scientific python stack: scipy (v.1.3.1)[63], numpy (v.1.17.2)[62], and matplotlib (v.3.1.1)[61]. All raw data and accompanying statistical analyses can be found in the extended data supplement.

Supplementary Material

Refer to Web version on PubMed Central for supplementary material.

ACKNOWLEDGMENTS

We are thankful for the assistance of Drs. Mathieu Bourdenx, with the proteomic analysis; Maryam Jafari, with organelle isolation; and Susmita Kaushik, with feedback and proofreading. This work was supported by NIH grants AG021904, AG054108, DK098408 (to A.M.C.), AG031782 (to A.M.C., L.S., and J.J.B.-C.), NS100717 (to A.M.C. and N.J.K.), NS095435 (to D.L.S.), R01CA244780 (to J.J.B.-C.), and P30-CA196521 (Tish Institute); NIH Shared Instrumentation Grant FAIN: S10OD021838 (to The Microscopy CoRE at Mount Sinai); and the Rainwaters and JPB Foundations (to A.M.C.). G.J.K. was supported by NIH training grants T32GM007288 and T32GM007491, B.S. by the German Academic Exchange Service, and P.K. by a DFG KI 1992/1-1 postdoctoral fellowship.

DECLARATION OF INTERESTS

A.M.C. is a co-founder and advisor to Selphagy (a Life Biosciences program) and consults for Generian Pharmaceuticals and Cognition Therapeuticals. The lab of N.J.K. has received support from Vir Biotechnology and F. Hoffmann-La Roche. N.J.K. consults for Mount Sinai, Maze Therapeutics, and Interline Therapeutics; is a shareholder in Tenaya Therapeutics; and has received stocks from Maze Therapeutics and Interline Therapeutics.

REFERENCES

1. Levine B, and Klionsky DJ (2017). Autophagy wins the 2016 Nobel Prize in Physiology or Medicine: Breakthroughs in baker's yeast fuel advances in biomedical research. Proc. Natl. Acad. Sci. USA 114, 201–205. [PubMed: 28039434]

2. Galluzzi L, Baehrecke EH, Ballabio A, Boya P, Bravo-San Pedro JM, Cecconi F, Choi AM, Chu CT, Codogno P, Colombo MI, et al. (2017). Molecular definitions of autophagy and related processes. EMBO J. 36, 1811–1836. [PubMed: 28596378]

3. Barbosa MC, Grosso RA, and Fader CM (2018). Hallmarks of Aging: An Autophagic Perspective. Front. Endocrinol. 9, 790.

4. Rubinsztein DC, Mariño G, and Kroemer G. (2011). Autophagy and aging. Cell 146, 682–695. [PubMed: 21884931]

5. López-Otín C, Blasco MA, Partridge L, Serrano M, and Kroemer G. (2013). The hallmarks of aging. Cell 153, 1194–1217. [PubMed: 23746838]

6. Menzies FM, Fleming A, Caricasole A, Bento CF, Andrews SP, Ashkenazi A, Füllgrabe J, Jackson A, Jimenez Sanchez M, Karabiyik C, et al. (2017). Autophagy and Neurodegeneration: Pathogenic Mechanisms and Therapeutic Opportunities. Neuron 93, 1015–1034. [PubMed: 28279350]

7. Scrivo A, Bourdenx M, Pampliega O, and Cuervo AM (2018). Selective autophagy as a potential therapeutic target for neurodegenerative disorders. Lancet Neurol. 17, 802–815. [PubMed: 30129476]

8. Mizushima N. (2020). The ATG conjugation systems in autophagy. Curr. Opin. Cell Biol. 63, 1–10. [PubMed: 31901645]

9. Arias E, and Cuervo AM (2020). Pros and Cons of Chaperone-Mediated Autophagy in Cancer Biology. Trends Endocrinol. Metabol. 31, 53–66.

10. Levine B. (2007). Cell biology: autophagy and cancer. Nature 446, 745–747. [PubMed: 17429391]

11. Feng Y, He D, Yao Z, and Klionsky DJ (2014). The machinery of macroautophagy. Cell Res. 24, 24–41. [PubMed: 24366339]

12. Kaushik S, and Cuervo AM (2018). The coming of age of chaperone-mediated autophagy. Nat. Rev. Mol. Cell Biol. 19, 365–381. [PubMed: 29626215]

13. Cuervo AM, and Dice JF (1996). A receptor for the selective uptake and degradation of proteins by lysosomes. Science 273, 501–503. [PubMed: 8662539]

14. Bandyopadhyay U, Kaushik S, Varticovski L, and Cuervo AM (2008). The chaperone-mediated autophagy receptor organizes in dynamic protein complexes at the lysosomal membrane. Mol. Cell Biol. 28, 5747–5763. [PubMed: 18644871]

15. Kunz JB, Schwarz H, and Mayer A. (2004). Determination of four sequential stages during microautophagy in vitro. J. Biol. Chem. 279, 9987–9996. [PubMed: 14679207]

16. Tekirdag K, and Cuervo AM (2018). Chaperone-mediated autophagy and endosomal microautophagy: Joint by a chaperone. J. Biol. Chem. 293, 5414–5424. [PubMed: 29247007]

17. Wang L, Klionsky DJ, and Shen HM (2023). The emerging mechanisms and functions of microautophagy. Nat. Rev. Mol. Cell Biol. 24, 186–203. [PubMed: 36097284]

18. Sahu R, Kaushik S, Clement CC, Cannizzo ES, Scharf B, Follenzi A, Potolicchio I, Nieves E, Cuervo AM, and Santambrogio L. (2011). Microautophagy of cytosolic proteins by late endosomes. Dev. Cell 20, 131–139. [PubMed: 21238931]

19. Morozova K, Clement CC, Kaushik S, Stiller B, Arias E, Ahmad A, Rauch JN, Chatterjee V, Melis C, Scharf B, et al. (2016). Structural and Biological Interaction of hsc-70 Protein with Phosphatidylserine in Endosomal Microautophagy. J. Biol. Chem. 291, 18096–18106. [PubMed: 27405763]

20. Caballero B, Bourdenx M, Luengo E, Diaz A, Sohn PD, Chen X, Wang C, Juste YR, Wegmann S, Patel B, et al. (2021). Acetylated tau inhibits chaperone-mediated autophagy and promotes tau pathology propagation in mice. Nat. Commun. 12, 2238. [PubMed: 33854069]

21. Cuervo AM, Knecht E, Terlecky SR, and Dice JF (1995). Activation of a selective pathway of lysosomal proteolysis in rat liver by prolonged starvation. Am. J. Physiol. 269, C1200–C1208. [PubMed: 7491910]

22. Juste YR, and Cuervo AM (2019). Analysis of Chaperone-Mediated Autophagy. Methods Mol. Biol. 1880, 703–727. [PubMed: 30610733]

23. Kaushik S, and Cuervo AM (2009). Methods to monitor chaperone-mediated autophagy. Methods Enzymol. 452, 297–324. [PubMed: 19200890]

24. Massey AC, Zhang C, and Cuervo AM (2006). Chaperone-mediated autophagy in aging and disease. Curr. Top. Dev. Biol. 73, 205–235. [PubMed: 16782460]
25. Schneider JL, Suh Y, and Cuervo AM (2014). Deficient chaperone-mediated autophagy in liver leads to metabolic dysregulation. Cell Metabol. 20, 417–432.
26. Schneider JL, Villarroya J, Diaz-Carretero A, Patel B, Urbanska AM, Thi MM, Villarroya F, Santambrogio L, and Cuervo AM (2015). Loss of hepatic chaperone-mediated autophagy accelerates proteostasis failure in aging. Aging Cell 14, 249–264. [PubMed: 25620427]
27. Caballero B, Wang Y, Diaz A, Tasset I, Juste YR, Stiller B, Mandelkow EM, Mandelkow E, and Cuervo AM (2018). Interplay of pathogenic forms of human tau with different autophagic pathways. Aging Cell 17, e12692. [PubMed: 29024336]
28. Uytterhoeven V, Lauwers E, Maes I, Miskiewicz K, Melo MN, Swerts J, Kuenen S, Wittocx R, Corthout N, Marrink SJ, et al. (2015). Hsc70–4 Deforms Membranes to Promote Synaptic Protein Turnover by Endosomal Microautophagy. Neuron 88, 735–748. [PubMed: 26590345]
29. Dong S, Aguirre-Hernandez C, Scrivo A, Eliscovich C, Arias E, Bravo-Cordero JJ, and Cuervo AM (2020). Monitoring spatiotemporal changes in chaperone-mediated autophagy in vivo. Nat. Commun. 11, 645. [PubMed: 32005807]
30. Koga H, Martinez-Vicente M, Macian F, Verkhusha VV, and Cuervo AM (2011). A photoconvertible fluorescent reporter to track chaperone-mediated autophagy. Nat. Commun. 2, 386. [PubMed: 21750540]
31. Kirchner P, Bourdenx M, Madrigal-Matute J, Tiano S, Diaz A, Bartholdy BA, Will B, and Cuervo AM (2019). Proteome-wide analysis of chaperone-mediated autophagy targeting motifs. PLoS Biol. 17, e3000301. [PubMed: 31150375]
32. Szklarczyk D, Gable AL, Nastou KC, Lyon D, Kirsch R, Pyysalo S, Doncheva NT, Legeay M, Fang T, Bork P, et al. (2021). Correction to 'The STRING database in 2021: customizable protein-protein networks, and functional characterization of user-uploaded gene/measurement sets'. Nucleic Acids Res. 49, 10800. [PubMed: 34530444]
33. Jassal B, Matthews L, Viteri G, Gong C, Lorente P, Fabregat A, Sidiropoulos K, Cook J, Gillespie M, Haw R, et al. (2020). The reactome pathway knowledgebase. Nucleic Acids Res. 48, D498–D503. [PubMed: 31691815]
34. Juste YR, Kaushik S, Bourdenx M, Aflakpui R, Bandyopadhyay S, Garcia F, Diaz A, Lindenau K, Tu V, GJ K, et al. (2021). Reciprocal regulation of chaperone-mediated autophagy and the circadian clock. Nat. Cell Biol. 23, 1255–1270. [PubMed: 34876687]
35. Hao Y, Kacal M, Ouchida AT, Zhang B, Norberg E, and Vakifahmetoglu-Norberg H. (2019). Targetome analysis of chaperone-mediated autophagy in cancer cells. Autophagy 15, 1558–1571. [PubMed: 30821613]
36. Bhave M, Mino RE, Wang X, Lee J, Grossman HM, Lakoduk AM, Danuser G, Schmid SL, and Mettlen M. (2020). Functional characterization of 67 endocytic accessory proteins using multiparametric quantitative analysis of CCP dynamics. Proc. Natl. Acad. Sci. USA 117, 31591–31602. [PubMed: 33257546]
37. Schröder B. (2016). The multifaceted roles of the invariant chain CD74 − More than just a chaperone. Biochim. Biophys. Acta 1863, 1269–1281. [PubMed: 27033518]
38. Agarraberes FA, and Dice JF (2001). A molecular chaperone complex at the lysosomal membrane is required for protein translocation. J. Cell Sci. 114, 2491–2499. [PubMed: 11559757]
39. Cuervo AM, Dice JF, and Knecht E. (1997). A population of rat liver lysosomes responsible for the selective uptake and degradation of cytosolic proteins. J. Biol. Chem. 272, 5606–5615. [PubMed: 9038169]
40. Ferreira JV, Fôfo H, Bejarano E, Bento CF, Ramalho JS, Girão H, and Pereira P. (2013). STUB1/CHIP is required for HIF1A degradation by chaperone-mediated autophagy. Autophagy 9, 1349–1366. [PubMed: 23880665]
41. Kawahara H, Minami R, and Yokota N. (2013). BAG6/BAT3: emerging roles in quality control for nascent polypeptides. J. Biochem. 153, 147–160. [PubMed: 23275523]
42. Abildgaard AB, Gersing SK, Larsen-Ledet S, Nielsen SV, Stein A, Lindorff-Larsen K, and Hartmann-Petersen R. (2020). Co-Chaperones in Targeting and Delivery of Misfolded Proteins to the 26S Proteasome. Biomolecules 10, 1141. [PubMed: 32759676]

43. Koga H, Kaushik S, and Cuervo AM (2010). Altered lipid content inhibits autophagic vesicular fusion. Faseb. J. 24, 3052–3065. [PubMed: 20375270]
44. Schuldner M, Dörsam B, Shatnyeva O, Reiners KS, Kubarenko A, Hansen HP, Finkernagel F, Roth K, Theurich S, Nist A, et al. (2019). Exosome-dependent immune surveillance at the metastatic niche requires BAG6 and CBP/p300-dependent acetylation of p53. Theranostics 9, 6047–6062. [PubMed: 31534536]
45. Klionsky DJ, and Emr SD (2000). Autophagy as a regulated pathway of cellular degradation. Science 290, 1717–1721. [PubMed: 11099404]
46. Olsvik HL, Svenning S, Abudu YP, Brech A, Stenmark H, Johansen T, and Mejlvang J. (2019). Endosomal microautophagy is an integrated part of the autophagic response to amino acid starvation. Autophagy 15, 182–183. [PubMed: 30295124]
47. Chiang HL, Terlecky SR, Plant CP, and Dice JF (1989). A role for a 70-kilodalton heat shock protein in lysosomal degradation of intracellular proteins. Science 246, 382–385. [PubMed: 2799391]
48. Elbaum-Garfinkle S, Ramlall T, and Rhoades E. (2010). The role of the lipid bilayer in tau aggregation. Biophys. J. 98, 2722–2730. [PubMed: 20513417]
49. Cuervo AM, Stefanis L, Fredenburg R, Lansbury PT, and Sulzer D. (2004). Impaired degradation of mutant alpha-synuclein by chaperone-mediated autophagy. Science 305, 1292–1295. [PubMed: 15333840]
50. Orenstein SJ, Kuo SH, Tasset I, Arias E, Koga H, Fernandez-Carasa I, Cortes E, Honig LS, Dauer W, Consiglio A, et al. (2013). Interplay of LRRK2 with chaperone-mediated autophagy. Nat. Neurosci. 16, 394–406. [PubMed: 23455607]
51. Kaushik S, and Cuervo AM (2015). Degradation of lipid droplet-associated proteins by chaperone-mediated autophagy facilitates lipolysis. Nat. Cell Biol. 17, 759–770. [PubMed: 25961502]
52. Blouin A, Bolender RP, and Weibel ER (1977). Distribution of organelles and membranes between hepatocytes and nonhepatocytes in the rat liver parenchyma. A stereological study. J. Cell Biol. 72, 441–455. [PubMed: 833203]
53. Zhang C, and Cuervo AM (2008). Restoration of chaperone-mediated autophagy in aging liver improves cellular maintenance and hepatic function. Nat. Med. 14, 959–965. [PubMed: 18690243]
54. Mejlvang J, Olsvik H, Svenning S, Bruun JA, Abudu YP, Larsen KB, Brech A, Hansen TE, Brenne H, Hansen T, et al. (2018). Starvation induces rapid degradation of selective autophagy receptors by endosomal microautophagy. J. Cell Biol. 217, 3640–3655. [PubMed: 30018090]
55. Mukherjee A, Patel B, Koga H, Cuervo AM, and Jenny A. (2016). Selective endosomal microautophagy is starvation-inducible in Drosophila. Autophagy 12, 1984–1999. [PubMed: 27487474]
56. Jacomin AC, Gohel R, Hussain Z, Varga A, Maruzs T, Eddison M, Sica M, Jain A, Moffat KG, Johansen T, et al. (2021). Degradation of arouser by endosomal microautophagy is essential for adaptation to starvation in Drosophila. Life Sci. Alliance 4, e202000965.
57. Schlundt A, Sticht J, Piotukh K, Kosslick D, Jahnke N, Keller S, Schuemann M, Krause E, and Freund C. (2009). Proline-rich sequence recognition: II. Proteomics analysis of Tsg101 ubiquitin-E2-like variant (UEV) interactions. Mol. Cell. Proteomics 8, 2474–2486. [PubMed: 19542561]
58. Stoorvogel W, Kleijmeer MJ, Geuze HJ, and Raposo G. (2002). The biogenesis and functions of exosomes. Traffic 3, 321–330. [PubMed: 11967126]
59. Zempel H, Thies E, Mandelkow E, and Mandelkow EM (2010). Abeta oligomers cause localized Ca(2+) elevation, missorting of endogenous Tau into dendrites, Tau phosphorylation, and destruction of microtubules and spines. J. Neurosci. 30, 11938–11950. [PubMed: 20826658]
60. Massey AC, Kaushik S, Sovak G, Kiffin R, and Cuervo AM (2006). Consequences of the selective blockage of chaperone-mediated autophagy. Proc. Natl. Acad. Sci. USA. 103, 5805–5810. [PubMed: 16585521]
61. Hunter JD (2007). Matplotlib: A 2D graphics environment. Comput. Sci. Eng. 9, 90–95.
62. van der Walt S, Colbert SC, and Varoquaux G. (2011). The NumPy Array: A Structure for Efficient Numerical Computation. Comput. Sci. Eng. 13, 22–30.
63. Jones E, Oliphant T, and Peterson P. (2001). SciPy (Open Source Scientific Tools for Python).

64. Deutsch EW, Csordas A, Sun Z, Jarnuczak A, Perez-Riverol Y, Ternent T, Campbell DS, Bernal-Llinares M, Okuda S, Kawano S, et al. (2017). The ProteomeXchange consortium in 2017: supporting the cultural change in proteomics public data deposition. Nucleic Acids Res. 45, D1100–D1106. [PubMed: 27924013]

65. Kampmann M, Bassik MC, and Weissman JS (2014). Functional genomics platform for pooled screening and generation of mammalian genetic interaction maps. Nat. Protoc. 9, 1825–1847. [PubMed: 24992097]

66. Wattiaux R, Wattiaux-De Coninck S, Ronveaux-dupal MF, and Dubois F. (1978). Isolation of rat liver lysosomes by isopycnic centrifugation in a metrizamide gradient. J. Cell Biol. 78, 349–368. [PubMed: 211139]

67. Krause GJ, and Cuervo AM (2021). Assessment of mammalian endosomal microautophagy. Methods Cell Biol. 164, 167–185. [PubMed: 34225914]

68. Storrie B, and Madden EA (1990). Isolation of subcellular organelles. Methods Enzymol. 182, 203–225. [PubMed: 2156127]

69. Kimura S, Noda T, and Yoshimori T. (2007). Dissection of the autophagosome maturation process by a novel reporter protein, tandem fluorescent-tagged LC3. Autophagy 3, 452–460. [PubMed: 17534139]

70. Lowry OH, Rosebrough NJ, Farr AL, and Randall RJ (1951). Protein measurement with the Folin phenol reagent. J. Biol. Chem. 193, 265–275. [PubMed: 14907713]

71. Schindelin J, Arganda-Carreras I, Frise E, Kaynig V, Longair M, Pietzsch T, Preibisch S, Rueden C, Saalfeld S, Schmid B, et al. (2012). Fiji: an open-source platform for biological-image analysis. Nat. Methods 9, 676–682. [PubMed: 22743772]

72. Meier F, Brunner AD, Koch S, Koch H, Lubeck M, Krause M, Goedecke N, Decker J, Kosinski T, Park MA, et al. (2018). Online Parallel Accumulation-Serial Fragmentation (PASEF) with a Novel Trapped Ion Mobility Mass Spectrometer. Mol. Cell. Proteomics 17, 2534–2545. [PubMed: 30385480]

73. Cox J, Hein MY, Luber CA, Paron I, Nagaraj N, and Mann M. (2014). Accurate proteome-wide label-free quantification by delayed normalization and maximal peptide ratio extraction, termed MaxLFQ. Mol. Cell. Proteomics 13, 2513–2526. [PubMed: 24942700]

74. Choi M, Chang CY, Clough T, Broudy D, Killeen T, MacLean B, and Vitek O. (2014). MSstats: an R package for statistical analysis of quantitative mass spectrometry-based proteomic experiments. Bioinformatics 30, 2524–2526. [PubMed: 24794931]

75. Pascovici D, Handler DCL, Wu JX, and Haynes PA (2016). Multiple testing corrections in quantitative proteomics: A useful but blunt tool. Proteomics 16, 2448–2453. [PubMed: 27461997]

76. Team RC (2018). R: A Language and Environment for Statistical Computing (R Foundation for Statistical Computing). https://www.R-project.org/.

77. Plaisier SB, Taschereau R, Wong JA, and Graeber TG (2010). Rank-rank hypergeometric overlap: identification of statistically significant overlap between gene-expression signatures. Nucleic Acids Res. 38, e169. [PubMed: 20660011]

78. Kani K. (2017). Quantitative Proteomics Using SILAC. Methods Mol. Biol. 1550, 171–184. [PubMed: 28188530]

79. Nesvizhskii AI, Keller A, Kolker E, and Aebersold R. (2003). A statistical model for identifying proteins by tandem mass spectrometry. Anal. Chem. 75, 4646–4658. [PubMed: 14632076]

Highlights

- CMA and eMI activities are upregulated in response to failure of each other
- A selective part of the CMA subproteome is rerouted to eMI upon CMA blockage
- Bag6 is required for substrate internalization by eMI
- Starvation inhibits eMI through changes in Bag6 dynamics in late endosomes

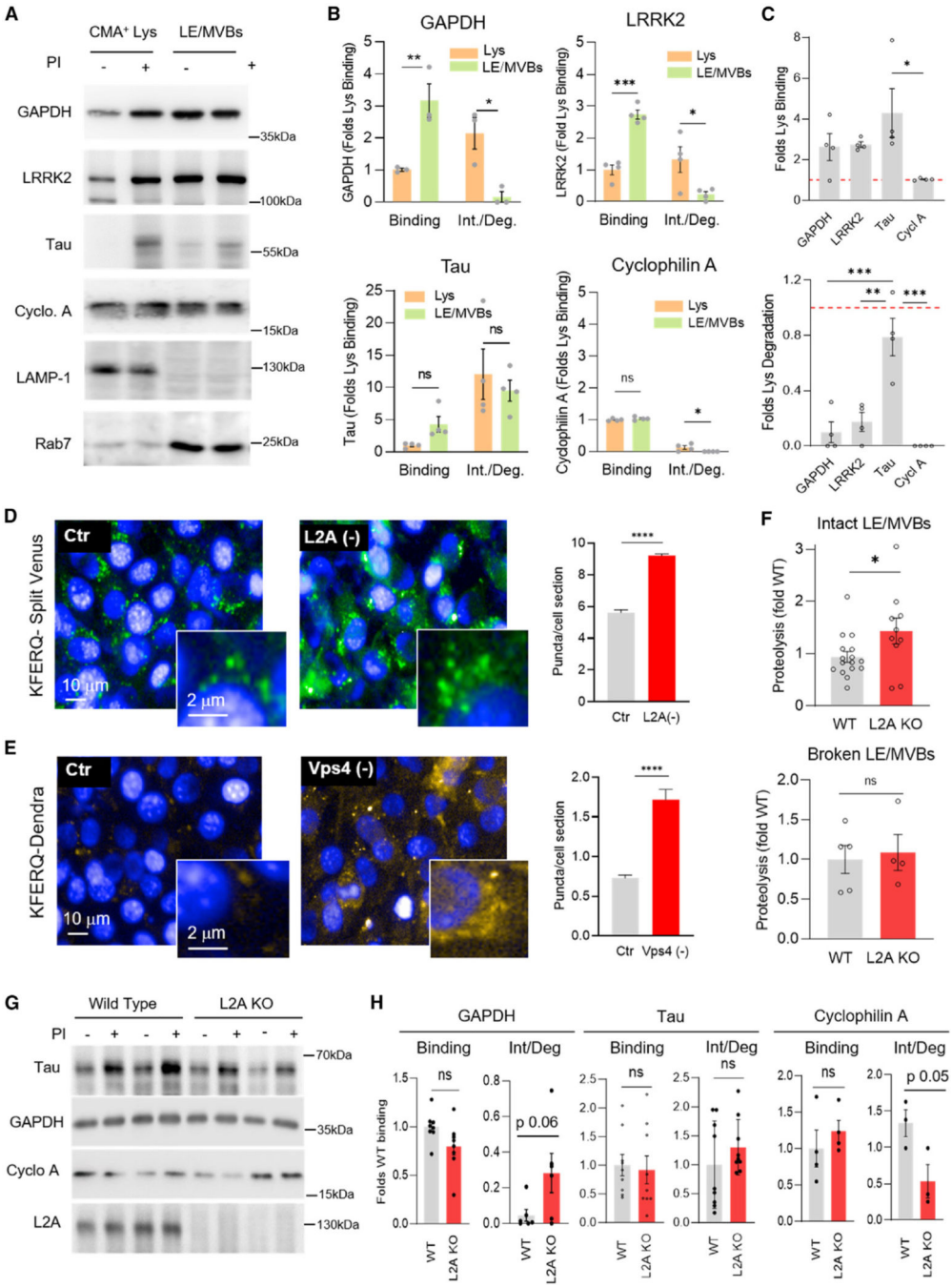

Figure 1. eMI and CMA share substrate proteins and display compensatory activity

(A–C) Immunoblot (A) of isolated rat liver lysosomes active for CMA (CMA$^+$ Lys) and late endosomes (LE/MVBs) treated or not with protease inhibitors (PI) and then incubated with the indicated proteins. LAMP-1 and Rab7 are used as compartment markers. Quantification of the amount of substrate bound and internalized or degraded (Int/Deg) (B) and ratio of binding (top) and Int/Deg (bottom) of the indicated substrates by LE/MVBs relative to lysosomes (C); n = 4 independent experiments.

(D) Representative images (left) and quantification (right) of eMI activity (as average number of fluorescent puncta per cell section) in mouse fibroblasts, control (Ctr) or knocked down for LAMP-2A (L2A(−)), stably expressing the KFERQ-Split Venus reporter to measure eMI. Nuclei are highlighted with Hoechst. Insets: higher-magnification images; n > 2,500 cells from three independent experiments.
(E) Representative images (left) and quantification (right) of CMA activity (as average number of fluorescent puncta per cell section) in mouse fibroblasts, control (Ctr) or knocked down for Vps4A/B (Vps4(−)), stably expressing the KFERQ-Dendra reporter to measure CMA. Nuclei are highlighted with Hoechst. Insets: higher-magnification images; n > 2,500 cells from three independent experiments.
(F) Proteolytic activity of intact (top) or detergent-disrupted (bottom) LE/MVBs isolated from wild-type (WT) and L2A-knockout (KO) mouse liver incubated with a pool of radiolabeled cytosolic proteins; n > 10 (intact) or 4 (broken) mice.
(G and H) Immunoblot (G) and quantification (H) of binding and internalization/degradation of the indicated proteins in LE/MVBs isolated from WT or L2AKO mouse liver; n = 8 (GAPDH), 9 (Tau), and 4 (Cyclophilin A) mice per genotype. Data are the mean ± SEM and individual values. Two-way ANOVA with Bonferroni's multiple comparisons *post hoc* test (B), one-way ANOVA with Tukey's multiple comparison *post hoc* test (C), and unpaired t test (D–H) were used. Significant differences: *p < 0.05, **p < 0.01, ***p < 0.001, and ****p < 0.0001. See also Figures S1 and S2.

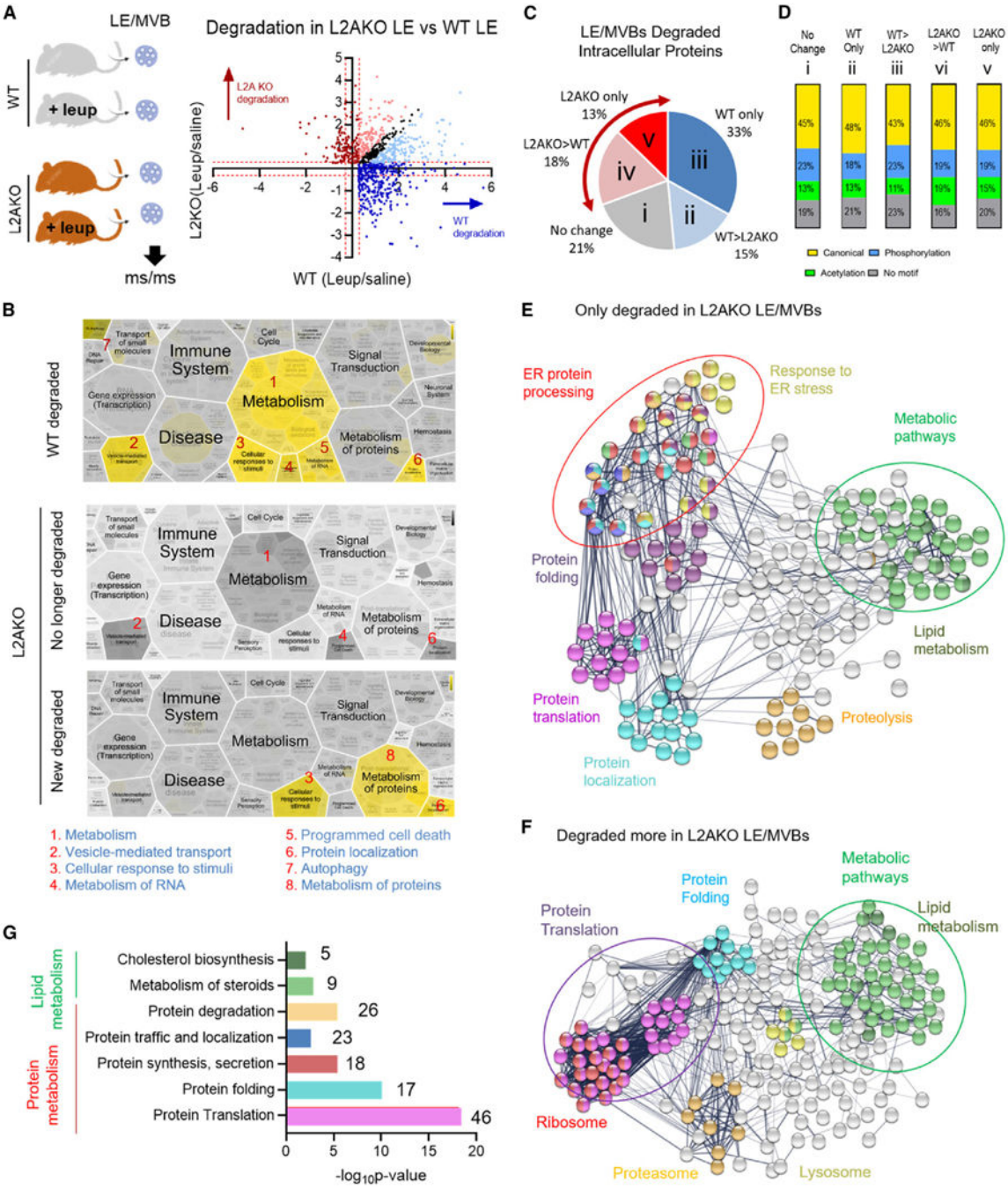

Figure 2. A subset of the proteome degraded by CMA is rerouted to eMI upon CMA failure

(A) Left: schematic of comparative proteomics of LE/MVBs isolated from livers of wild-type (WT) and LAMP-2A knockout (L2AKO) mice injected or not with leupeptin (Leup) to block LE/MVB degradation. Right: $\log_2$ fold change ($\log_2$FC) in rates of protein degradation in LE/MVBs in WT compared with L2AKO. Black, proteins equally degraded in both groups; blue, reduced (light) or absent (dark) degradation in L2AKO; red, increased (light) or only (dark) degradation in L2AKO.

(B) Voronoi flattened visualization using REACTOME pathway analysis of intracellular proteins undergoing degradation in LE/MVBs from WT mouse livers (top) and proteins no longer degraded or only degraded in LE/MVBs from L2AKO mice (bottom).
(C) Percentage of LE/MVB proteins undergoing degradation only or at a higher rate in L2AKO (L2AKO > WT) mice is marked as the potentially rerouted proteome (red arrow). Roman numerals indicate the groups described in the text.
(D) Analysis of KFERQ-like motifs in the protein groups in (C).
(E–G) STRING analysis (E and F) and functional families with enrichment (G) of proteins displaying exclusive or higher degradation in LE/MVBs from L2AKO mice. All GO terms are statistically enriched, with $p < 0.001$. See also Figure S3.

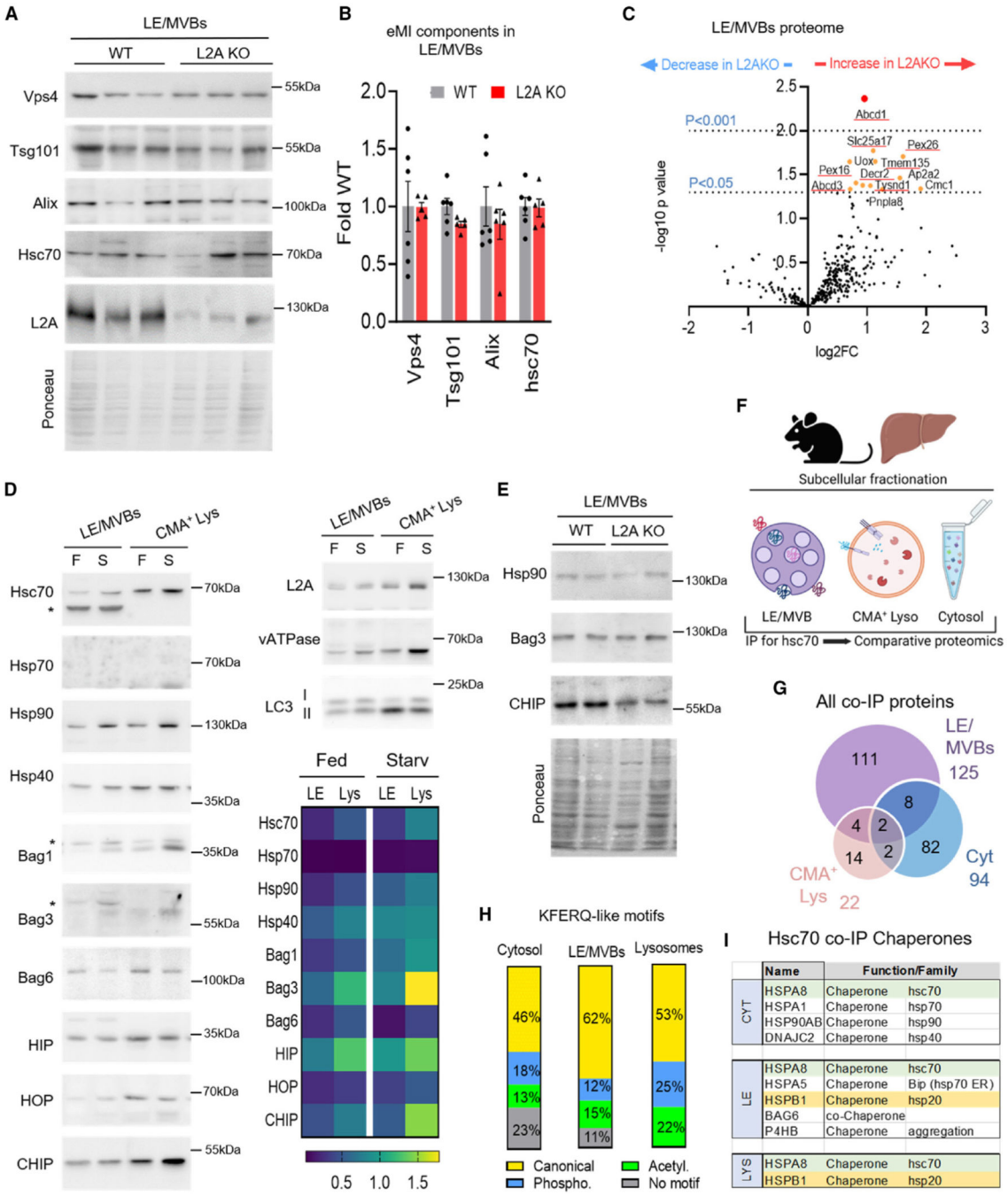

Figure 3. Changes in CMA activity are associated with discrete remodeling of the LE/MVB proteome

(A and B) Immunoblot (A) and quantification (B) for the indicated proteins of LE/MVBs isolated from livers of wild-type (WT) and LAMP-2A knockout (L2AKO) mice; n = 6 mice. The residual LAMP-2A band in L2AKO mice is due to cross-reactivity of the antibody with other LAMP-2 isoforms; these mice have no LAMP-2A mRNA.[25]

(C) Volcano plot showing $\log_2$ fold change ($\log_2$FC) of levels of non-substrate LE/MVB proteins between WT and L2AKO mice against their negative $\log_{10}$-transformed p values. Names of proteins with significantly higher levels in L2AKO LE/MVBs are shown.

(D) Immunoblot for chaperones and co-chaperones in LE/MVBs and CMA^+ lysosomes isolated from livers of fed (F) or 48-h-starved (S) rats. Top right: markers of endolysosomes. Bottom right: heatmap of the abundance of the indicated proteins from quantification of immunoblots on the left; n = 3 rats per group.

(E) Immunoblot of LE/MVBs from livers of WT and L2AKO mice for the indicated chaperones.

(F–I) Co-immunoprecipitation of proteins with Hsc70 from LE/MVBs, CMA^+ lysosomes, and cytosol. Experimental schematic (F), Venn diagram of proteins recovered in the immunoprecipitation of each compartment (G), percentage of KFERQ-like motifs in those proteins (H), and table of identified chaperones (I). Ponceau staining is shown as a loading control in (A) and (E). Data in (B) are the mean ± SEM and individual values. Multiple t test did not reveal statistical differences. See also Figures S4 and S5 and Table S1.

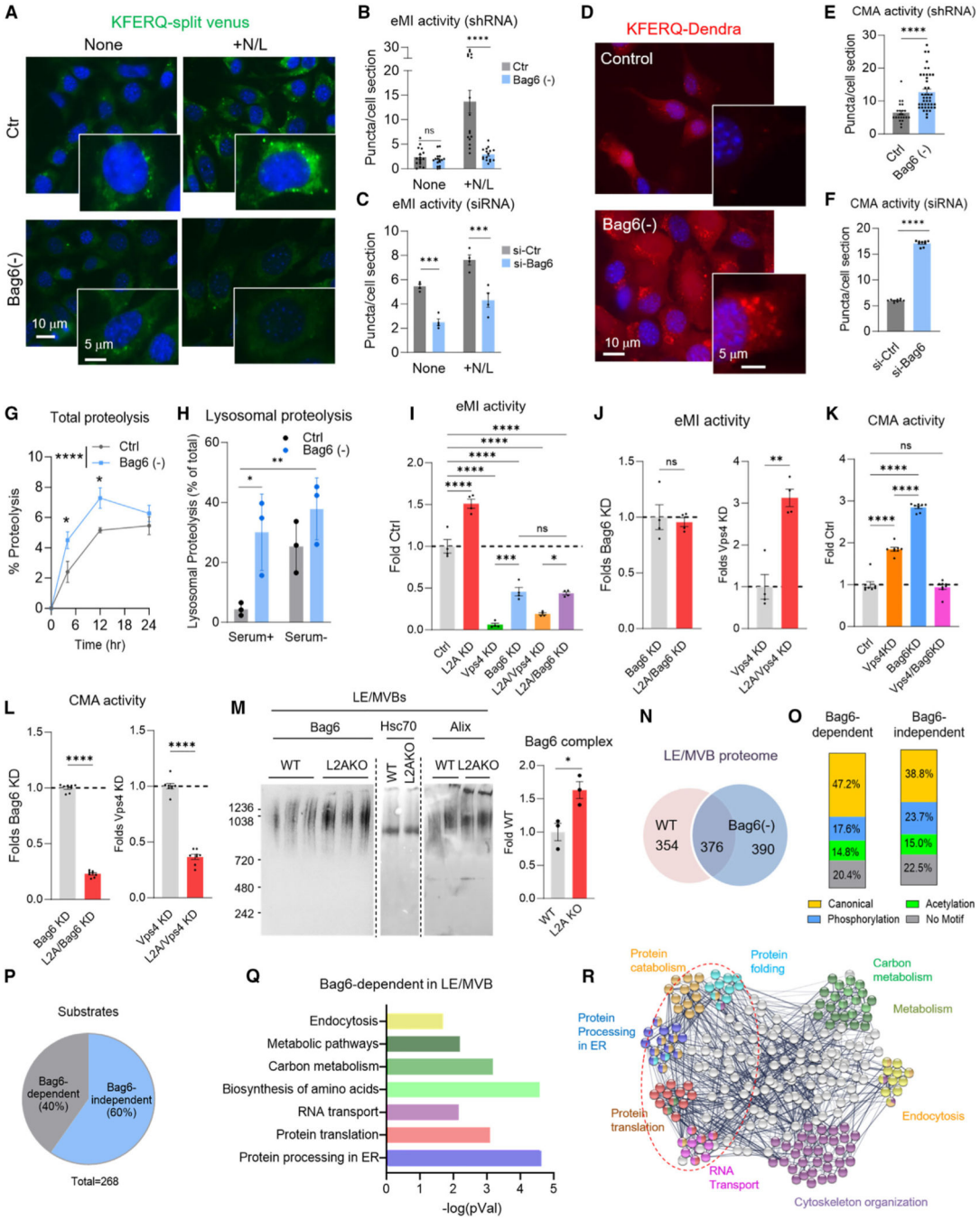

Figure 4. Bag6 is required for eMI degradation of a subset of the proteome

(A–C) Representative images (A) and quantification (B and C) of eMI activity in NIH3T3 mouse fibroblasts stably expressing the KFERQ-Split Venus reporter control (Ctr) or knocked down (−) for Bag6 using shRNA (A and B) or siRNA (C). Where indicated, cells were treated with ammonium chloride and leupeptin (+N/L) to block degradation. Nuclei are highlighted with DAPI. Insets: higher magnification images; n = 16 fields from four independent experiments for (B) and n > 2,500 cells from four independent experiments (C).

(D–F) Representative images (D) and quantification (E and F) of CMA activity in NIH3T3 mouse fibroblasts stably expressing the KFERQ-Dendra reporter Ctr or knocked down (−) for Bag6 using shRNA (D and E) or siRNA (D). Nuclei are highlighted with DAPI. Insets: higher magnification images; n > 30 cells from four independent experiments (E) and n > 2,500 cells from four independent experiments (F).

(G and H) Degradation of long-lived proteins in Ctr and Bag6(−) NIH3T3 fibroblasts. Rates of total (G) and endolysosomal (H) protein degradation are shown; n = 3 independent experiments.

(I–L) Quantification of eMI activity (I and J) or CMA activity (K and L) using NIH3T3 mouse fibroblasts stably expressing the KFERQ-Split Venus reporter or KFERQ-Dendra reporter, respectively, upon the indicated knockdowns (KD). Data in (I) and (K) are relative to values in control cells. Data in (J) and (L) are relative to the indicated single KD; n > 2,500 cells from four (I and J) or eight or nine (K and L) independent experiments.

(M) Representative immunoblots of Bag6 (left), Hsc70 (middle), and Alix (right) after blue native electrophoresis of WT and LAMP-2A KO LE/MVBs. Samples were run in the same gel, and dotted lines indicate where the membrane was cut to blot for each protein separately. Quantification of the high-molecular-weight form of Bag6 is shown on the right; n = 3 independent experiments.

(N–R) Comparative proteomics of LE/MVBs isolated from Ctr and Bag6(−) cells. Venn diagram of proteins in both groups (N), presence of KFERQ-like motifs (O), fraction of the LE/MVB proteome degraded in a Bag6-dependent or -independent manner (P), functional families with protein enrichment in the group of proteins detected only in LE/MVBs in the presence of Bag6 (Q), and STRING analysis of the same proteins (R). Data in (B), (C), (E), (F), and (G)–(M) are the mean ± SEM and individual values. Two-way ANOVA with Bonferroni's (B, C, and G) or Tukey's (H) multiple comparisons *post hoc* test, unpaired t test (E, F, J, L, and M), and one-way ANOVA with Bonferroni's multiple comparisons *post hoc* test (I and K) were used. Significant differences: *$p < 0.05$, **$p < 0.01$, ***$p < 0.001$, ****$p < 0.0001$. All GO terms in (Q) are statistically enriched, with $p < 0.05$. See also Figure S5 and Tables S1 and S2.

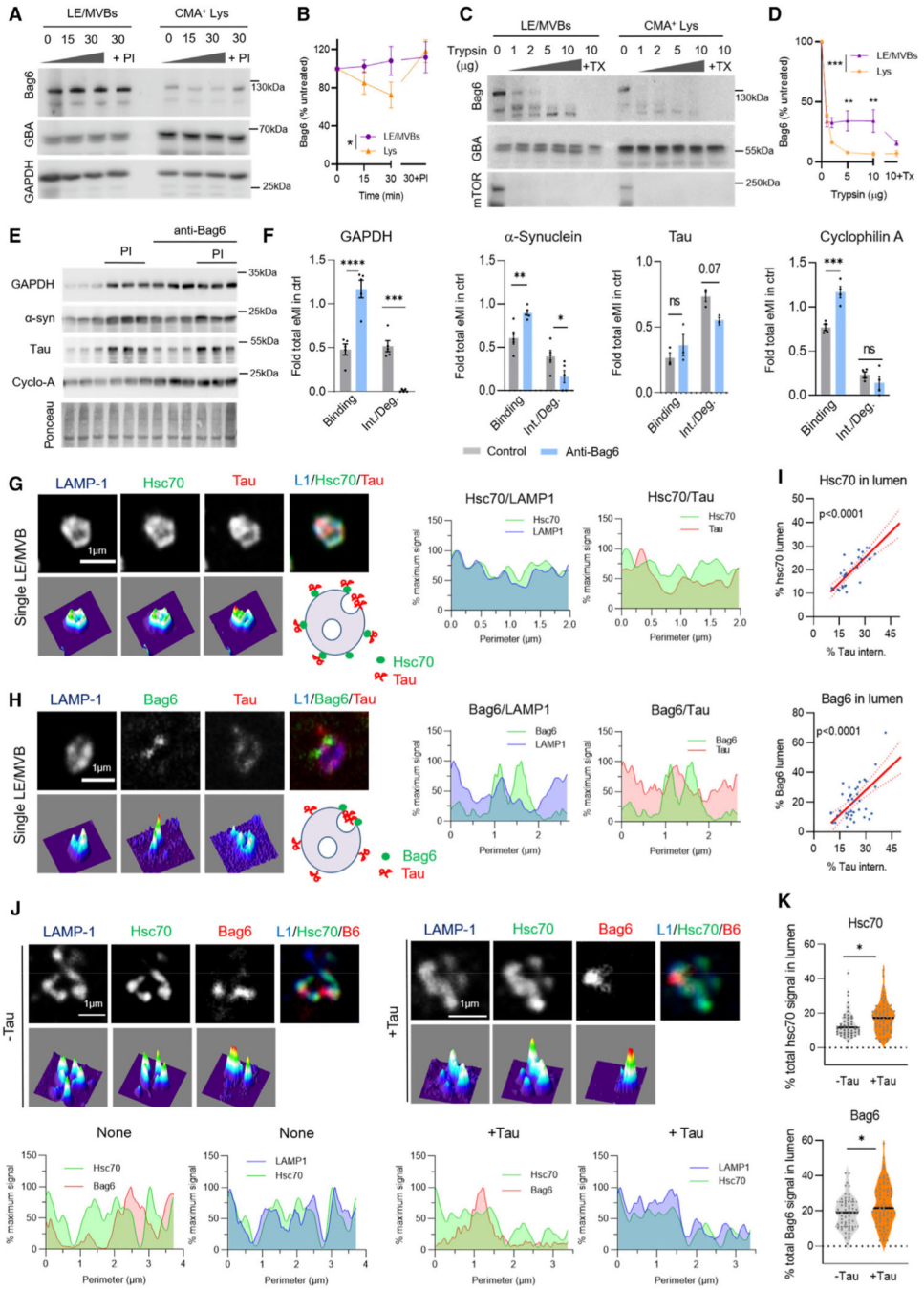

Figure 5. LE/MVB-associated Bag6 is required for eMI

(A and B) Organelle stability of Bag6. Representative immunoblots (A) of LE/MVBs and CMA-active (CMA^+) lysosomes incubated at 37°C for the indicated times with or without protease inhibitors (PI) with examples of constitutive (GBA) and substrate proteins (GAPDH). The percentage of Bag6 remaining in each compartment at the indicated times is shown in (B); n = 3 independent experiments.

(C and D) Organelle topology of Bag6. Representative immunoblots (C) and quantification (D) of LE/MVBs and CMA^+ lysosomes incubated with increasing concentrations of trypsin

only or with Triton X-100 (TX) to facilitate access to luminal proteins. GBA and mTOR are shown as examples of luminal and membrane-associated proteins, respectively. The percentage of Bag6 relative to the untreated samples is shown in (D); n = 3 independent experiments.

(E and F) Representative immunoblots (E) and quantification (F) of LE/MVBs preincubated or not with PI and/or an antibody against Bag6 (anti-Bag6) and then incubated with the indicated substrates. Ponceau staining is shown as a loading control. Data are presented relative to the total amount of substrate protein detected in samples incubated with PI but not the antibody; n = 5 (GAPDH, α-syn), 3 (Tau), and 4 (Cyclophilin A) independent experiments.

(G–I) Representative Tau-STED microscopy images of isolated LE/MVBs incubated with Tau and immunolabeled for the indicated proteins (G and H, left); single-channel images (top) and 2.5D density plots (bottom) (G and H). Examples of fluorescence coincidence signals and intensity plotting of each signal along the perimeter of the organelles (G and H, right). Schemes on the right show proposed topology for the indicated proteins. The linear correlations between luminal content of Hsc70 (top) and Bag6 (bottom) with Tau internalization are shown in (I); n = 3 animals, ≥30 LE/MVBs per condition.

(J and K) Representative Tau-STED microscopy images of isolated LE/MVBs incubated with or without Tau and immunolabeled for the indicated proteins; single-channel images (J, top) and 2.5D density plots (J, middle). Examples of fluorescence coincidence signals and intensity plotting of each signal along the perimeter of the organelles are shown in (J), bottom. Percentage of Hsc70 (K, top) and Bag6 (K, bottom) in the lumen of LE/MVBs incubated in the presence (+) or absence (−) of Tau; n = 5 animals, ≥50 LE/MVBs per condition. Data are the mean ± SEM and individual values. Two-way ANOVA with Bonferroni's multiple comparisons *post hoc* test (B, C, D, and F) and unpaired t test (K) were used. Simple linear regression was used in (I). Significant differences: *$p < 0.05$, **$p < 0.01$, ***$p < 0.001$, ****$p < 0.0001$; ns, not significant. See also Figure S6.

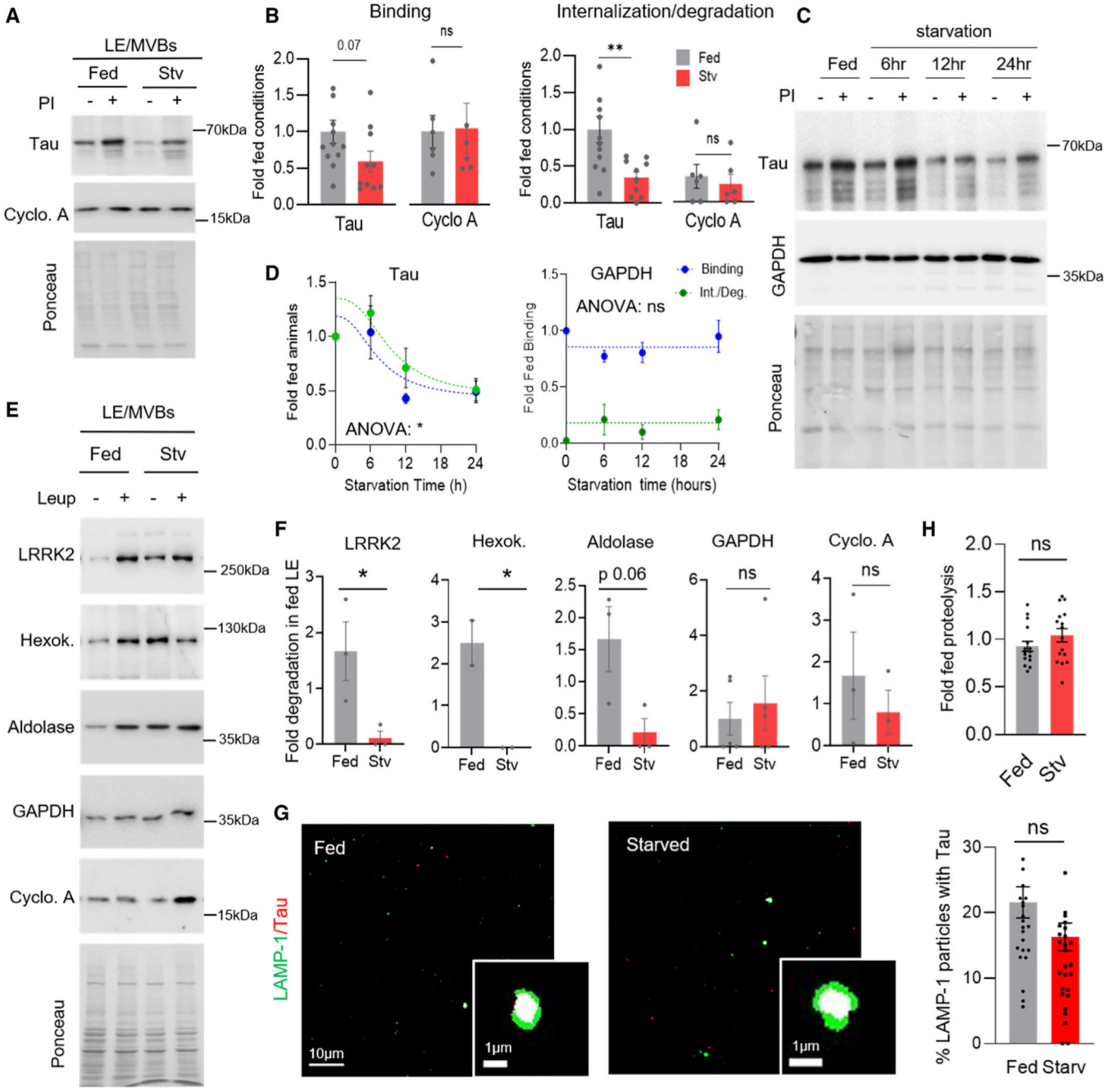

Figure 6. eMI activity is inhibited by the absence of nutrients

(A and B) Immunoblot of LEs/MVBs isolated from livers of fed or 24-h-starved (Stv) rats treated or not with protease inhibitors (PI) and then incubated with the indicated proteins (A). Quantification of the amount of substrate protein bound (B, left) and internalized/degraded (B, right) relative to fed conditions; n = 10 (Tau) and 6 (Cyclophilin A) independent experiments.

(C and D) Immunoblot (B) and quantification (C) of LE/MVBs isolated from livers of rats fed or starved for the indicated periods of time and incubated with Tau (left) or GAPDH (right) as in (A). Values are expressed relative to fed rats; n = 4 independent experiments.

(E and F) Representative immunoblot for the indicated proteins (E) and quantification (F) of LE/MVBs isolated from livers of fed and 24-h-starved (Stv) rats injected or not with leupeptin to block LE/MVB degradation. Data are expressed relative to degradation in LE/MVBs from fed mice; n = 4 (GAPDH), 3 (LRRK2, aldolase, Cyclophilin A), or 2 (hexokinase) rats.

(G) Left: representative confocal images of LE/MVBs isolated from fed or 24-h-starved rats and immunostained for the indicated proteins after incubating with Tau. Inset: overlapping mask (in white) of higher-magnification image. Right: quantification of the percentage of co-localization; n ≥ 25 fields from three independent experiments.

(H) Proteolytic activity of detergent-disrupted LE/MVBs isolated from livers of fed or 24-h-starved rats incubated with a pool of radiolabeled cytosolic proteins. Values are expressed relative to those in fed rats; n = 16 independent experiments. Ponceau staining is shown in (A), (C), and (E) as a loading control. Data are the mean ± SEM and individual values. Two-way ANOVA (D) and unpaired t test (B, F, and H) were used. Significant differences: *$p < 0.05$ and **$p < 0.01$; ns, not significant. See also Figure S7.

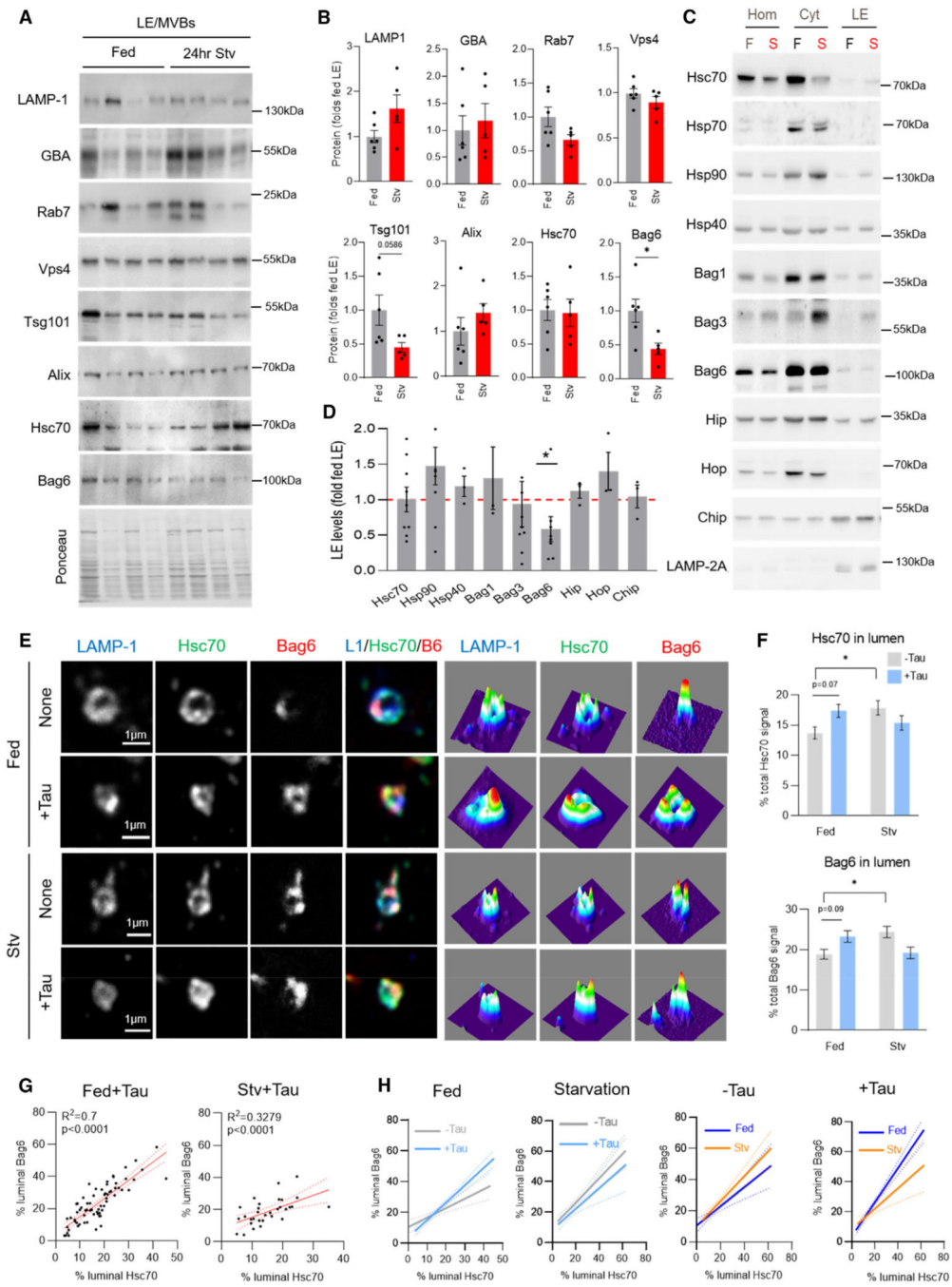

Figure 7. Starvation changes levels and topology of LE/MVB-associated Bag6

(A and B) Representative immunoblot for the indicated proteins (A) and quantification (B) of LE/MVBs isolated from livers of fed or 24-h-starved rats. Ponceau staining is shown as loading control; n = 6 (Fed) and 5 (Stv) rats.

(C and D) Representative immunoblot for the indicated chaperones (C) and quantification (D) in homogenates (Hom), cytosol (Cyt), and LE/MVBs (LE) isolated from livers of fed (F) or 24-h-starved (S) rats. Values in (D) are expressed relative to average fed levels; n = 3–9 rats.

(E–H) Representative STED microscopy images of LE/MVBs isolated from fed or 24-h-starved mouse livers incubated or not with Tau and immunolabeled for the indicated proteins. Single-channel images (left) and 2.5D density plots for each one (right) are shown (E). Quantification of the percentage of each protein present in the LE/MVB lumen (F) and correlation between luminal Hsc70 and Bag6 levels per LE/MVB from fed and starved mice (G) and overlapped correlations between both chaperones in the same LE/MVB samples as in (E) to illustrate the effect of starvation (left) or of incubation with Tau (right) (H); n = 3 animals, ≥30 LE/MVBs per condition. Data are the mean ± SEM and individual values. Unpaired (B) and one-sample multiple (D) t test and two-way ANOVA with Tukey's multiple comparisons *post hoc* test (F) were used. Simple linear correlations were used in (G) and (H). Significant difference: *$p < 0.05$; ns, not significant. See also Figure S7.

KEY RESOURCES TABLE

REAGENT or RESOURCE	SOURCE	IDENTIFIER
Antibodies		
goat anti-mouse IgG 594 ATTO	Rockland	Cat# 610–155-121; RRID:AB_10893162
goat anti-rabbit IgG 594 ATTO	Sigma	Cat# 77671–1ML-F
goat anti-mouse IgG 647 ATTO	Sigma	Cat# 50185–1ML-F
goat anti-rabbit IgG 647N ATTO	Rockland	Cat# 611–156-122; RRID:AB_10893043
goat anti-rabbit IgG HRP	KPL	Cat# 5067202
goat anti-mouse IgG HRP	KPL	Cat# 5067205
goat anti-mouse IgM HRP	Jackson Immunoresearch	Cat# 115–035-075; RRID:AB_2338508
rabbit anti-sheep IgG HRP	SeraCare/KPL	Cat# 5220–0372
donkey anti-goat IgG HRP	Jackson Immunoresearch	Cat# 705–035-003; RRID:AB_2340390
Donkey anti-rat IgG HRP	Jackson Immunoresearch	Cat# 712–035-150; RRID:AB_2340638
donkey anti-sheep 647	Thermo	Cat # A-21448; RRID: AB_2535865
donkey anti-goat 647	Thermo	Cat # A32849; RRID: AB_2762840
goat anti-rat 488	Thermo	Cat # A-11006; RRID: AB_2534074
goat anti-mouse 488	Thermo	Cat # A-10680; RRID: AB_2534062
goat anti-mouse 555	Thermo	Cat # A32727; RRID: AB_2633276
goat anti-mouse 647	Thermo	Cat # A-21235; RRID: AB_2535804
goat anti-rabbit 555	Thermo	Cat # A32732; RRID: AB_2633281
donkey anti-rabbit 647	Thermo	Cat # A-31573; RRID: AB_2536183
rabbit anti-Aldolase	Cell Signaling	Cat # 3188s; RRID:AB_2226674
Rabbit anti-Alix	Novus	Cat # NBP1–90201; RRID:AB_11023702
mouse anti- Alix (3A9)	Cell Signaling	Cat # 2171S; RRID:AB_2299455
mouse anti-α Synuclein (211)	Santa Cruz	Cat # sc-12767
rabbit anti-ATP6V1B	Abcam	Cat # ab200839
rabbit anti-Bag1	Abcam	Cat # ab32109; RRID:AB_2062445
rabbit anti-Bag3	Novus	Cat # NBP2–27398SS
sheep anti-Bag6	R&D Systems	Cat # AF6438; RRID:AB_10717417
rabbit anti-Bag6	Abcam	Cat # ab137076
rabbit anti-Cathepsin B	Abcam	Cat # ab214428; RRID:AB_2848144

REAGENT or RESOURCE	SOURCE	IDENTIFIER
mouse anti-Cathepsin D (D-7)	Santa Cruz	Cat # sc-377299; RRID:AB_2827539
rabbit anti-Cathepsin L (H-80)	Santa Cruz	Cat # sc-10778; RRID:AB_2087827
rabbit anti-CHIP (C3B6)	Cell Signaling	Cat # 2080; RRID:AB_2198052
rabbit anti-Cyclophilin A	Cell Signaling	Cat # 2175; RRID:AB_2169116
mouse anti-EEA-1	BD Biosciences	Cat # 610456; RRID: AB_397830
rabbit anti-GAPDH	Cell Signaling	Cat # 2118s; RRID:AB_561053
rabbit anti-GBA	Sigma	Cat # G4171; RRID:AB_1078958
rabbit anti-Hexokinase	Cell Signaling	Cat # 2024s; RRID:AB_2116996
rabbit anti-HIP	Stressgen	Cat # adi-spa-766; RRID:AB_10618971
rabbit anti-HOP	Enzo	Cat # adi-sra-1500; RRID:AB_10618972
mouse anti-hsc70 (13D3)	Novus	Cat # nb120–2788; AB_2120309
rabbit anti-hsc70/hsp70	Enzo	Cat # ADI-SPA-757; RRID:AB_10616383
rabbit anti-hsp40	Assay Designs	Cat # adi-spa-410; AB_10615088
rabbit anti-hsp90	Stressgen	Cat # ADI-SPA-835-F; RRID:AB_11181205
rat anti-LAMP-1 (1D4B)	Hybridoma bank	Cat # 1D4B; RRID: AB_2134500
mouse anti-LAMP-1 (LyC16)	Enzo	Cat # adi-vam-en001; RRID:AB_10630197
rabbit anti-LAMP-2A	Thermo Fisher	Cat # 512200; RRID: AB_2533900
rabbit anti-LC3	Cell Signaling	Cat # 2775; RRID: AB_915950
rabbit anti-LRRK2 (MJFF3)	Abcam	Cat # ab133475; RRID:AB_2620136
rabbit anti-mTOR	Cell Signaling	Cat # 2972; RRID:AB_330978
mouse anti-p62	Abcam	Cat # ab56416; RRID:AB_945626
rabbit anti-Rab7 (D95F2)	Cell Signaling	Cat # 9367; RRID:AB_1904103
Rabbit anti-Tau Y9	Enzo	Cat # BML-TA3119–0100; RRID:AB_11181753
mouse anti-Total Tau (DA9)	Dr. Peter Davies	Zempel et al., 2010[59]; RRID:AB_2716723
rabbit anti-Tsg101	Abcam	Cat # ab30871; RRID:AB_2208084
mouse anti-tubulin	Sigma	Cat # T7451; RRID:AB_609894
rabbit anti-Ubiquitin	Dako	Cat # Z0458; RRID: AB_2315524
rabbit normal IgG	Cell Signaling	Cat # 2729S; RRID:AB_1031062
mouse anti-Vps4 (E-8)	Santa Cruz	Cat # sc-133122; RRID:AB_2304400
Chemicals, peptides, and recombinant proteins		

REAGENT or RESOURCE	SOURCE	IDENTIFIER
α-synuclein	rPeptide	Cat # S-1001–2
Tau-441	rPeptide	Cat # T-1001–2
LRRK2	Thermo Fisher	Cat # PV4873
GAPDH	Sigma	Cat # G2267
Cyclophilin A	R&D systems	Cat # 3589-CA-100
Ammonium Chloride	Sigma-Aldrich	Cat # A9434
DMEM	Sigma-Aldrich	Cat # D5648
Hoechst 33342	ThermoFisher Scientific	Cat # H3570
Leupeptin (animal injection)	Sigma-Aldrich	Cat # L5793
Newborn Calf Serum	Atlanta Biologicals	Cat # S11250
Pierce ECL Western Blotting Substrate	Thermo Fisher Scientific	Cat #32106
Prolong Diamond Anti-fade Mountant	ThermoFisher Scientific	Cat # P36961
Leupeptin (cell culture)	ThermoFisher Scientific	Cat # BP2662–25
Opti-MEM	Life Technologies	Cat # 31985–062
Lipofectamine RNAiMAX	Life Technologies	Cat # 13778150
Ready Strip IPG Strips, pH 4–7	Bio-Rad	Cat # 1632001
L-Lysine-2HCl, 13C6, 15N2 for stable isotope labeling by amino acids in cell culture (SILAC)	ThermoFisher	Cat # 88432
Powdered RPMI Media for SILAC	ThermoFisher	Cat # 88426
L-Leucine, 13C6 for SILAC	ThermoFisher	Cat # 88435
Experimental models: Cell lines		
NIH-3T3	ATCC	Cat # CRL-1658; RRID:CVCL_0594
Deposited data		
Raw and analyzed data	This paper	N/A
LE/MVB WT and L2A KO proteomics	PRIDE repository	Identifier #: PXD029580
Hsc70 IP proteomics	PRIDE repository	Identifier #: PXD046797
WT and Bag6 KD LE/MVB proteomics	PRIDE repository	Identifier #: PXD046760
Experimental models: Organisms/strains		
Mouse: LAMP-2A$^{flox/flox}$	(Schneider et al., 2014)[25]	N/A

REAGENT or RESOURCE	SOURCE	IDENTIFIER
Oligonucleotides		
Empty vector	Millipore-Sigma	Cat # SHC001
shRNA-Bag6	Mission-Sigma library (Sigma Aldrich)	CCTATTATCCAGCAGGACATT RHS3979–9576316
shRNA-LAMP-2A	Made in-house (Massey et al., 2006[60])	CACCGCTGCAATCTGATTGATTAT CGAAATAATCAATCAGATTGCAG
siRNA-Vps4A	Mission-Sigma library (Sigma Aldrich)	TRCN0000101417
siRNA Vps4B	Mission-Sigma library (Sigma Aldrich)	TRCN0000101821
LAMP-2A Forward primer	In house	GCAGTGCAGATGAAGACAAC
LAMP-2A reverse primer	In house	AGTATGATGGCGCTTGAGAC
Bag6 siRNA	Dharmacon	Cat # J-045300–05 to −08
Software and algorithms		
STRING analysis v11.5	Szklarczyk et al., 2021[32]	String-db.org; RRID:SCR_005223
Reactome	Jassal et al., 2020[33]	Reactome.org; SCR_003485
KFERQ-finder	Kirchner et al., 2019[31] https://doi.org/10.1371/journal.pbio.3000301	https://rshine.einsteinmed.org/
LAS AF Lite	Leica	http://www.leica-microsystems.com; RRID:SCR_013673
Matplotlib 3.1.1	Hunter et al. 2007[61]	MatPlotLib; RRID: SCR_008624
Numpy 1.17.2	Van der Walt et al. 2011[62]	NumPy; RRID: SCR_008633
Python 3.7.4	Python Software Foundation	Python Programming Language; RRID: SCR_008394
SciPy 1.3.1	Jones et al. 2001[63]	SciPy; RRID: SCR_008058
GraphPad	Prism	http://www.graphpad.com/; RRID:SCR_002798
Adobe Photoshop 6.0	Adobe Systems	www.adobe.com; RRID:SCR_014199
AxioVision Rel. 4.8	Carl Zeiss	www.zeiss.com; RRID:SCR_002677
Colocalization Plugin (ImageJ)	NIH	https://imagej.nih.gov/ij/plugins/colocalization.html
Fiji	NIH	http://fiji.sc/ RRID:SCR_002285

REAGENT or RESOURCE	SOURCE	IDENTIFIER
Other		
Axiovert 200 with ApoTome .2 system fluorescence microscope	Carl Zeiss, Albert Einstein College of Medicine	www.zeiss.com
Fujifilm LAS-3000 Imager	Fujifilm, Albert Einstein College of Medicine	http://www.fujifilm.com/products/medical/
Operetta system	Perkin Elmer, Albert Einstein College of Medicine	https://www.perkinelmer.com/fr/product/operetta-cls-system-hh16000000
SP8-LIA confocal microscope	Leica Microsystems, Albert Einstein College of Medicine	http://www.leica-microsystems.com
Leica TCS SP8 STED 3X microscope	Leica Microsystems, Icahn School of Medicine at Mt. Sinai	https://www.leica-microsystems.com/products/confocal-microscopes/p/leica-tcs-sp8-sted-one/